PLOS CLIMATE

RESEARCH ARTICLE

# Daytime land surface temperature and its limits as a proxy for surface air temperature in a subtropical, seasonally wet region

**Nkosi Muse**[1,2]*, **Amy Clement**[3], **Katharine J. Mach**[1,2]

**1** Department of Environmental Science and Policy, Rosenstiel School of Marine, Atmospheric, and Earth Science, University of Miami, Miami, Florida, United States of America, **2** Leonard and Jayne Abess Center for Ecosystem Science and Policy, University of Miami, Coral Gables, Florida, United States of America, **3** Department of Atmospheric Sciences, Rosenstiel School of Marine, Atmospheric, and Earth Science, University of Miami, Miami, Florida, United States of America

* nkosi.muse@earth.miami.edu





**Citation:** Muse N, Clement A, Mach KJ (2024) Daytime land surface temperature and its limits as a proxy for surface air temperature in a subtropical, seasonally wet region. PLOS Clim 3(10): e0000278. https://doi.org/10.1371/journal.pclm.0000278

**Editor:** Ahmed Kenawy, Mansoura University, EGYPT

**Received:** July 17, 2023

**Accepted:** July 23, 2024

**Published:** October 2, 2024

**Peer Review History:** PLOS recognizes the benefits of transparency in the peer review process; therefore, we enable the publication of all of the content of peer review and author responses alongside final, published articles. The editorial history of this article is available here: https://doi.org/10.1371/journal.pclm.0000278



**Data Availability Statement:** All data used in this study is publicly available and sources are cited. Dates of Landsat 8 Level 2, Collection 1 satellite

## Abstract

Land surface temperatures (LSTs) captured via satellite remote sensing are widely used as a proxy for the surface air temperatures (SATs) experienced outdoors, a key component of human heat exposure. However, LST's accuracy in capturing SAT can vary through space and time across climate types and geographies and has been less explored in subtropical, seasonally wet regions (where summer precipitation exceeds 570 mm). Utilizing daytime (11 AM/12 PM local time, ET/EST) Landsat 8 remote sensing data, this study derived LST and evaluated its spatiotemporal patterns, as well as its relationship with SAT retrieved from local weather stations, using the case of Miami-Dade County, Florida, USA. Over 2013–2022, a surface urban heat island effect is distinctly present (mean SUHII = 3.43˚C)—most intense during spring months rather than summer months (mean spring SUHII = 4.09˚C). As such, LST peaks in May/June as opposed to July/August for many other parts of the northern hemisphere. In contrast, Miami-Dade SAT is greatest in August, and the strength of its relationship with LST varies by season. LST and SAT are most correlated in winter ($R$ = 0.91) and spring ($R$ = 0.59) months and least correlated during the wetter fall ($R$ = 0.40) months. The relationship between LST and SAT during the summer is statistically insignificant. In this subtropical region with a seasonally wet climate, LST effectively reflects the spatial heterogeneity of the urban thermal landscape, consistent with the literature across urban regions globally. However, because the strength of the LST-SAT relationship considerably weakens during wet season months, LST data therefore have limits as a proxy for the heat exposure people experience outdoors annually, as they may not accurately represent the magnitude of localized potential heat risks. These findings underscore important considerations in using LST data to identify urban heat exposures and inform potential adaptive responses in seasonally wet, subtropical-to-tropical regions.

imagery collected from EarthExplorer for this study can be found in S1 Table.

**Funding:** This research was funded by the McKnight Doctoral Fellowship Program of the Florida Education Fund (NM); the Rosenstiel School of Marine, Atmospheric, and Earth Science at the University of Miami (NM, AC, KJM); and the University of Miami Laboratory for Integrative Knowledge (U-LINK) (NM, AC, KJM). The funders had no role in study design, data collection and analysis, decision to publish, or preparation of the manuscript.

**Competing interests:** The authors have declared that no competing interests exist.

## 1. Introduction

Spatially explicit heat-hazard data are important in informing adaptive responses to reduce risks to human health and well-being [1, 2]. This is of increased relevance in rapidly expanding urban regions, where heat exposure and its heterogeneity are further amplified [3–6]. Because land surface temperature (LST) can be captured at high resolutions across large regions, highlighting the heterogeneity of thermal landscapes such as the surface urban heat island (SUHI), LST data have served useful in identifying potential heat exposures [7–25]. Such usefulness is largely attributed to the physical relationship that LST shares with that of surface air temperature (SAT), a measure that is representative of the ambient temperature that humans feel and a key component of heat exposure [5, 6]. Although controlled by different physical mechanisms and properties, LST and SAT have been found to be well correlated both temporally and spatially—for example, SATs are higher where LSTs are higher due to heat fluxes from the surface, and LST and SAT follow similar annual patterns [4, 5, 7, 26–35]. Therefore, LST, generally derived from satellite observations, has been widely used as a spatiotemporal proxy for SAT [26, 36–44]. However, LST's strength as such a proxy can vary across space and time [18, 33, 34, 37, 45–57].

In lower-latitude urban regions that experience seasonally wet, tropical climates (where summer precipitation exceeds 570 mm), the quantitative relationship between LST and SAT has been less explored [16, 58–60]. This gap is notable given different physical processes that operate at lower latitudes (e.g., increased solar radiation, more intense water cycle, etc.), as compared to more arid or temperate climates that have strong LST-SAT correlations year-round [19, 33, 55, 56]. The presence of such physical processes may affect LST's accuracy as a predictor for SAT values [1, 7, 34]. Thus, it cannot be simply assumed that LST can serve as a year-round proxy for SAT in lower-latitude regions with seasonally wet climates, informing decisions around heat exposures and appropriate heat responses. Although heat hazards in such a region are a function of more than SAT alone (e.g., increased water vapor/humidity), the LST-SAT relationship remains key to spatial heat exposure. For example, a lower atmosphere that is heated by the increased heat fluxes of a warm surface allows for a moister air mass and the potential for exacerbated heat stress [60, 61]. Identifying the strength of the LST-SAT relationship throughout the course of the year in a region with a seasonally wet, tropical climate is important for determining its ability to accurately quantify areas of potential increased heat risks. If LST and SAT are weakly correlated at a point in time annually (e.g., during the wet season or dry season), then LST may misrepresent the magnitude of a potential heat hazard across the seasonal cycle. Such a misrepresentation of heat exposure profiles could misinform appropriate, spatially explicit heat responses and adaptation strategies.

Here, we examine the spatiotemporal relationship between LST and SAT in a subtropical, seasonally wet region. We use the case of Miami-Dade County—a large, densely populated metropolitan region within subtropical latitudes that experiences a seasonally wet climate and possesses a unique geography. We ask: what is the spatiotemporal accuracy of daytime LST as a proxy for SAT in Miami-Dade? First, we develop a climatology of daytime LST (11 AM/12 PM local time, Eastern Time/Eastern Standard Time) over 2013–2022, as has not been done before for the region. Second, using this new LST record, we assess spatial patterns in LST, quantifying the surface urban heat island (SUHI) phenomenon and its seasonality. Third, we examine the spatiotemporal relationship between daytime LST and SAT. We thereby uncover strengths and limitations in using LST data to identify spatiotemporal urban heat exposures, based on its relationship with SAT in a subtropical, seasonally wet region. Such results are of increasing relevance to urban planning and heat adaptation policy, where accurate tools are needed to measure localized urban heat hazards under intensifying climate change.

## 2. Materials and methods

### 2.1. Study area

Miami-Dade County, Florida, USA, a large metropolitan region bordering the southern limit of subtropical latitudes, was chosen as the area of study (Fig 1). Miami-Dade is the state of Florida's third largest county by total area (2,431 square miles) and largest by population (2,701,767 people) [62]. Located in Southeast Florida, the county is bordered by the Atlantic Ocean to the east and the Everglades wetlands to the west. The wetlands account for the majority of Miami-Dade's total area and extend beyond the county's western border. Urban development, encroaching on wetlands over time, has increased Miami-Dade County's urban build up from 12% to 21% of the region's total area between 2001 and 2016, following global urbanization trends [3, 23]. To the south is the Caribbean Sea and the Florida Keys archipelago. Miami-Dade is characterized by a Tropical Monsoon (Am) climate closest to the Atlantic Ocean and a Tropical Savanna (Aw) climate further inland to the southwest [63].

On average, Miami-Dade is the warmest county within the state of Florida and contains the state's second warmest city (City of Miami, second warmest mean annual SATs statewide after Key West) [67]. During August, Miami-Dade SATs are at their highest on average annually (Fig 2A) [67–69]. The county's newly designated heat season begins May 1 and continues until

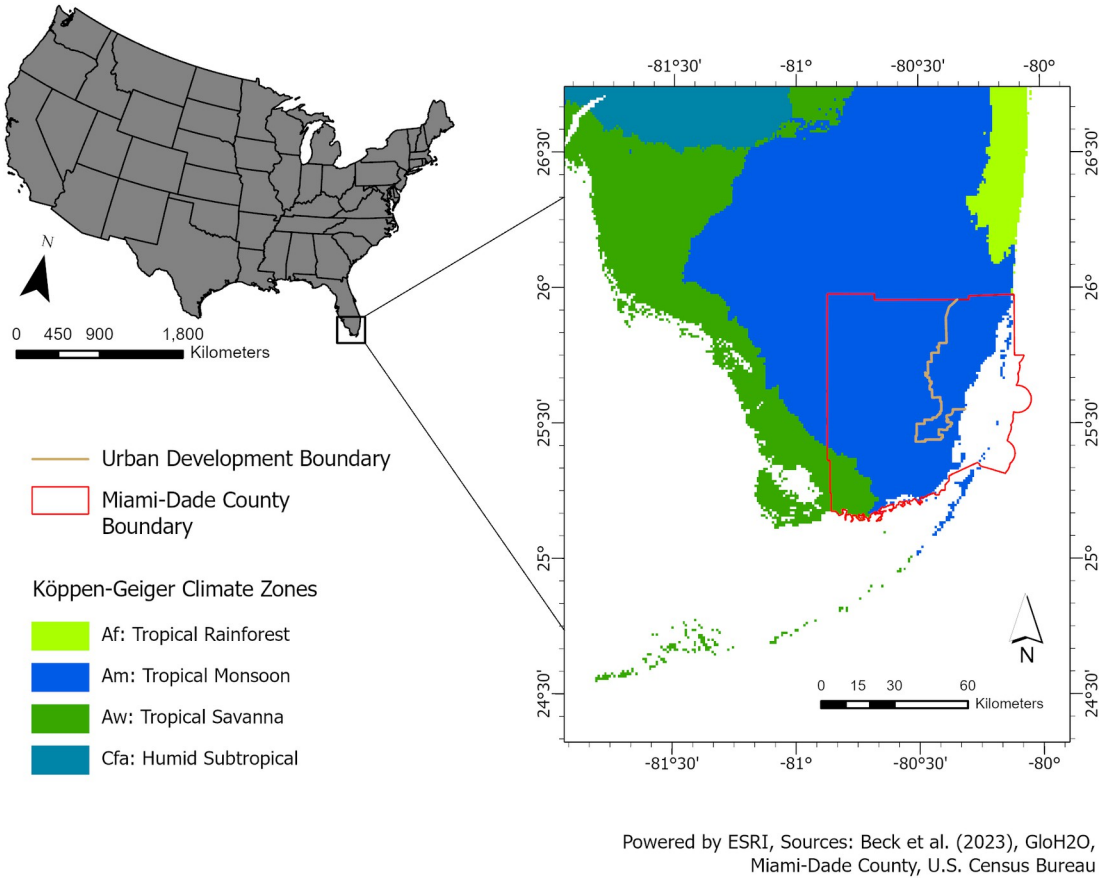


**Fig 1. A map of the study area, Miami-Dade County, in Southeast Florida, USA and its Köppen-Geiger Climate Zones [63].** The county's urban development boundary separates developed, urban Miami-Dade from the rural, Everglades wetlands to the west. USA shapefile: U.S. Census Bureau [64]. Miami-Dade County boundary shapefile, Urban development boundary shapefile: Miami-Dade County [65]. Climate zone map: GloH2O [66].

https://doi.org/10.1371/journal.pclm.0000278.g001

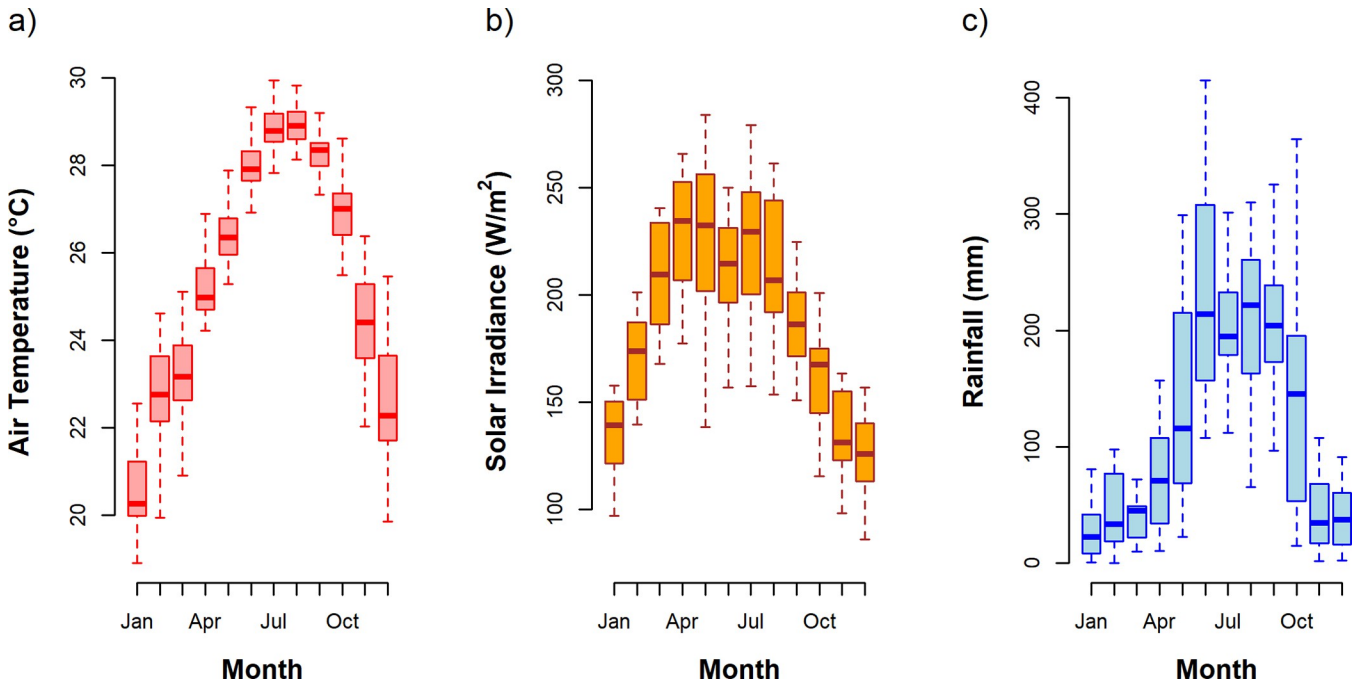


**Fig 2. Monthly SAT (˚C), surface solar irradiance (W/m$^2$), and rainfall (mm) for Miami-Dade County.** Box and whiskers display the 1$^{st}$, 25$^{th}$, 75$^{th}$, and 99$^{th}$ percentiles of each variable for each month. The box line represents the median. (a) Plotted values represent hourly SAT observations averaged by month for seven weather stations (6 WeatherSTEM [70] and Miami International Airport) during 2015–2022 ($n$ = 56 values per month). (b) Plotted values represent hourly solar irradiance observations (daytime, 7 am to 7 PM ET/EST) averaged by month for six WeatherSTEM stations during 2015–2022 ($n$ = 48 values per month). (c) Plotted values represent monthly model estimates from PRISM [71, 72] of local rainfall totals within a 4-km grid centered at Miami International Airport (KMIA) for each month during 2000–2020 ($n$ = 21 values per month).

https://doi.org/10.1371/journal.pclm.0000278.g002

the end of October, a period during which SATs can remain well above 25˚C, both during the day and at night. Closely aligned with the period of Miami-Dade's heat season is the Southeast Florida rainy season (Fig 2C). Although incoming solar radiation is highest in June, surface solar radiation does not simultaneously peak (Fig 2B).

## 2.2. Datasets description

Upgraded Level 2 LST data were retrieved from the National Aeronautics and Space Administration (NASA) and United States Geological Survey (USGS) Landsat 8 satellite, captured by the Operational Land Imager (OLI) and Thermal Infrared Sensor (TIRS) instruments. Landsat observations have higher resolutions, than other satellite products for urban surface thermal analysis (e.g., MODIS and Sentinel have 1-km resolutions) [73]. The Landsat 8 satellite orbits Earth on a 16-day cycle, capturing images of the planet's surface and providing data at 30-meter resolution [74]. Data from the satellite were downloaded by individual recorded day from the USGS Earth Explorer website [75], packaged with GeoTIFF images that represent each satellite band, the quality assessment (QA) band, and a metadata (MTL) file containing satellite thermal constants, rescaling factors, and corrections. Miami-Dade County falls within Path 15, Row 42 of the Worldwide Reference System (WRS-2) [76]. Images were captured at approximately 11 AM ET/12 PM EST during the satellite overpass. 260 total image scenes exist in the USGS Landsat 8 database for this region during 2013–2022. Miami-Dade County was obscured by cloud cover or intense moisture in 159 of these 260 images. Of the 101 non-obscured images downloaded across the ten-year study period (2013–2022), 98 were utilized

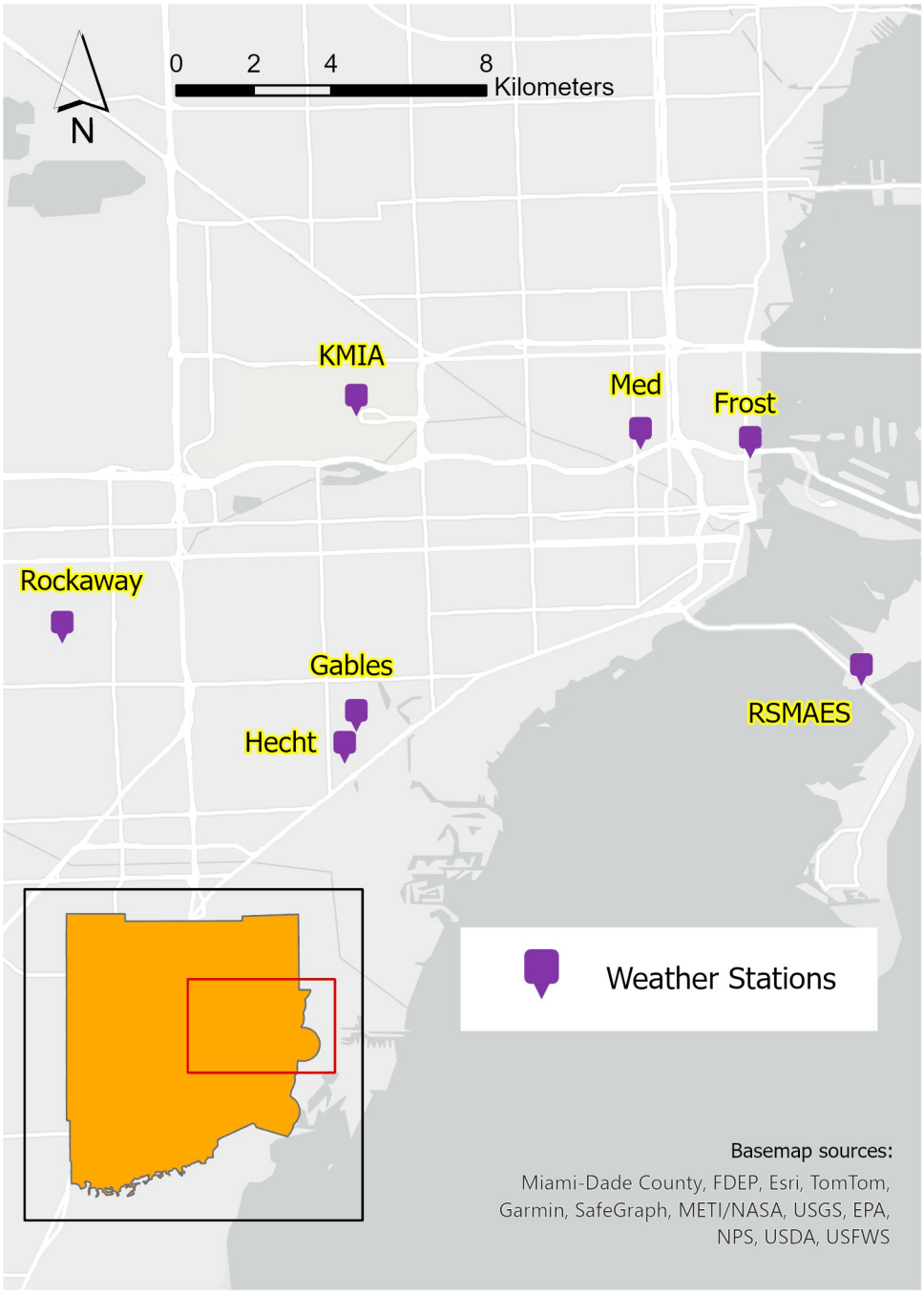


**Fig 3. Seven weather stations utilized for SAT observations.** Miami-Dade County shapefile: Miami-Dade County [65]. Basemap: ESRI [78, 79].

https://doi.org/10.1371/journal.pclm.0000278.g003

for analysis after an additional 3 were discarded due to missing data. The dates of utilized scenes are shown in S1 Table.

SATs were gathered for spatiotemporal analysis during 2015–2022 across seven different weather stations within the bounds of Miami-Dade County (Fig 3). Six of the seven stations

are WeatherSTEM stations: Frost Science Museum; Rockaway Middle School; Rosenstiel School of Marine, Atmospheric, and Earth Science (RSMAES); University of Miami Gables campus; University of Miami Medical campus; and University of Miami Hecht Athletic Center. Solar irradiance data (Fig 2) were also gathered at WeatherSTEM stations. Each WeatherSTEM station collects various atmospheric data continuously at one-minute intervals [70]. SAT data from the seventh station, Miami International Airport (KMIA), were retrieved from the Iowa State University ASOS Network [77]. Monthly rainfall total estimates (2000–2020) for Miami-Dade County (Fig 2) were retrieved from the Parameter-elevation Relationships on Independent Slopes Model (PRISM) [71, 72].

Census block group data for Miami-Dade County ($n$ = 1842) were retrieved from the U. S. Census Bureau [64]. Impervious surface and tree canopy data were retrieved from the National Land Cover Database (NLCD) at 30-meter resolution [80]. The value of each 30-by-30-meter pixel represents the percentage of developed surface or tree canopy for that area (0–100%).

## 2.3. Methodology

To first determine seasonal trends in LST, an annual climatology of mean LST was developed over a ten-year period (2013–2022) [81]. Spatial assessment of LST then involved the identification of the Miami-Dade SUHI phenomenon and its intensity (SUHII) across seasons, as well as drivers of intraurban heterogeneity. Lastly, the seasonal and annual patterns of LST were compared with SAT to determine whether the two measures of temperature remain highly spatiotemporally correlated in a seasonally wet climate. Fig 4 briefly highlights these three primary research objectives.

**2.3.1. LST mapping through time.** Through a series of calculations based on equations provided by USGS [42, 74, 82], downloaded Landsat 8 imagery data were converted to LST utilizing ArcGIS Pro's raster calculator [83]. Band 10 captured by the TIRS was used for mapping surface temperature, as it is less contaminated with stray light than Band 11 [84]. The steps for calculating LST include (1) determination of top-of-atmosphere (TOA) spectral radiance ($L_\lambda$), (2) conversion to TOA brightness temperature ($BT$), (3) calculation of land surface emissivity ($\varepsilon_\lambda$), and (4) the final calculation of LST. TOA spectral radiance is calculated in W/(m$^2$ × sr × μm) via:

$$L_\lambda = M_L \times Q_{cal} + A_L - O_i \tag{1}$$

where $M_L$ is the band-specific multiplicative rescaling factor, $Q_{cal}$ is the quantized and calibrated standard product pixel value measured in DNs, $A_L$ is the band-specific additive rescaling factor, and $O_i$ is the band-specific correction constant (Table 1). Next is the calculation of TOA $BT$, in degrees Celsius (˚C):

$$BT = \frac{K_2}{ln[(K_1/L_\lambda) + 1]} - 273.15, \tag{2}$$

Where $K_1$ and $K_2$ are band-specific thermal conversion constants in W/(m$^2$ × sr × μm) and Kelvin (K), respectively. The absolute zero (-273.15˚C) is added to convert from Kelvin to degrees Celsius. To calculate land surface emissivity ($\varepsilon_\lambda$), the proportion of vegetation ($P_v$) is first required. $P_v$ is calculated with the Normalized Difference Vegetation Index (NDVI) [85], utilizing Bands 4 and 5 captured by the Landsat 8 OLI:

$$\mathrm{NDVI} = \frac{Band\ 5 - Band\ 4}{Band\ 5 + Band\ 4},\ P_v = \left(\frac{\mathrm{NDVI} - \mathrm{NDVI}_{min}}{\mathrm{NDVI}_{max} - \mathrm{NDVI}_{min}}\right)^2.$$

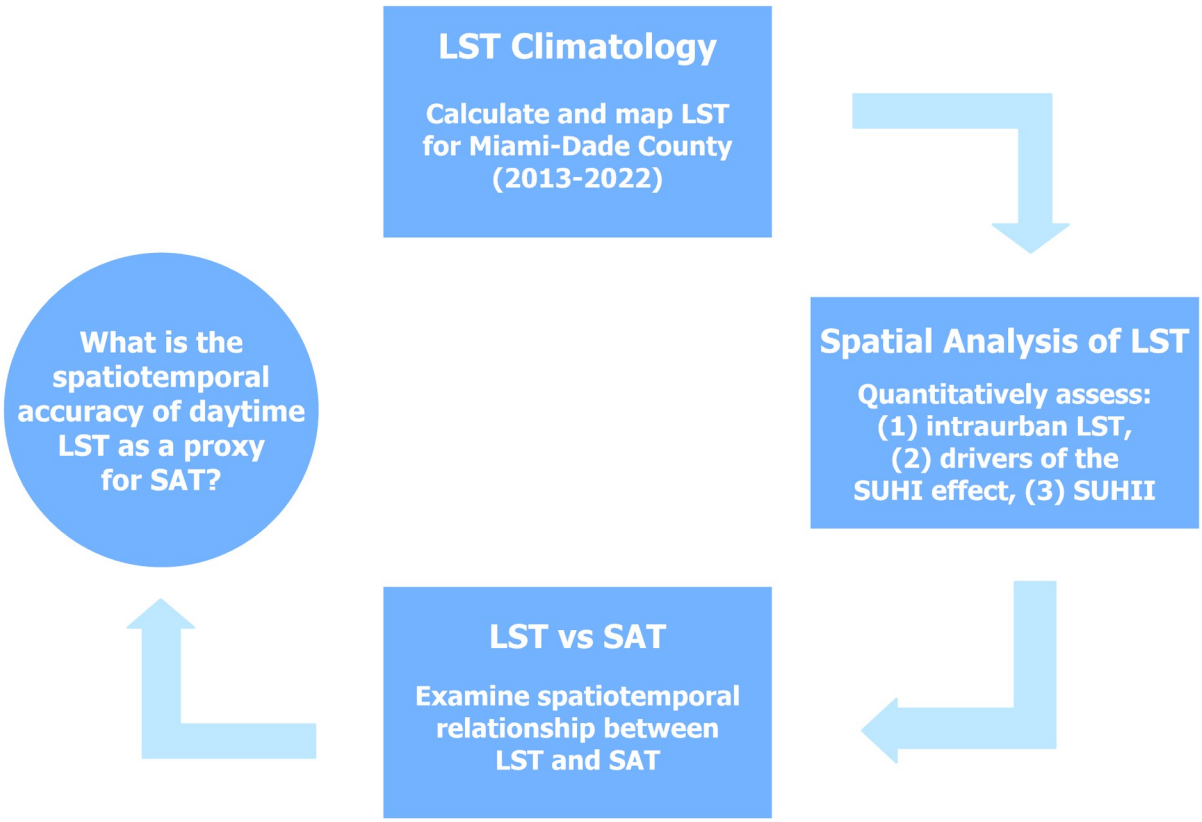


**Fig 4.** A flowchart of the study's three primary steps: (1) develop LST climatology, (2) spatially analyze the LST record, and (3) examine the relationship between LST and SAT.

https://doi.org/10.1371/journal.pclm.0000278.g004

$\varepsilon_\lambda$ can now be calculated via:

$$\varepsilon_\lambda = 0.004 \times P_v + 0.986, \tag{3}$$

a key component of the final LST equation:

$$\mathrm{LST} = \frac{BT}{\left[1 + \left(\frac{\lambda BT}{\rho}\right)\ln\left(\varepsilon_\lambda\right)\right]}, \tag{4}$$

**Table 1. Landsat 8 metadata.**

| | |
|---|---|
| **Thermal Conversion Constants** | |
| $K_1$ | 774.89 W/(m$^2$ × sr × μm) |
| $K_2$ | 1321.08 K |
| **Rescaling Factors** | |
| $M_L$ | 0.000342 |
| $A_L$ | 0.1 |
| **Correction Constant** | |
| $O_i$ | 0.29 |

https://doi.org/10.1371/journal.pclm.0000278.t001

with

$$\rho = h\frac{c}{\sigma},$$

where λ is the wavelength of the emitted radiance (λ = 10.895 μm), $h$ is Planck's constant (6.626 × 10−34 J s), $c$ is the speed of light (2.998 × $10^8$ m $s^{-1}$), and $\sigma$ is Boltzmann's constant (1.38 × 10−23 J $K^{-1}$). $\rho$ is converted to μm ×˚C to obtain LST in˚C.

All images were cloud and water masked using the Landsat Quality Assessment (QA_PIXEL) band. Pixel values within the QA_PIXEL band that did not possess a value of 21824, indicative of land [86], were removed (masked) from imagery.

**2.3.2. Spatial analysis of LST.** SUHI intensity (SUHII), or the difference between urban and rural LSTs [19, 29, 45, 54, 87, 88], was calculated for the overall daytime LST climatology (annual mean SUHII for 2013–2022) and seasonally (mean winter, spring, summer, and fall SUHII). Mean imperviousness was aggregated to the census block group level to determine urban or rural status. Census block groups were deemed urban ($n$ = 1826) if mean imperviousness was greater than or equal to 5%. This definition aligns with the Census Bureau urban-rural criteria (if a census block or block group falls within census tracts with a population greater than 2500) [89] and with the county's urban development boundary [90] (if a census block group falls east of the boundary, Fig 1). Remaining census block groups were considered rural ($n$ = 16) (Fig 5). Spatial analysis was conducted in ArcGIS Pro software [83].

**2.3.3. Statistical analysis.** Linear regression was performed in RStudio [91] to compare annual mean LST to common drivers of urban heat: NDVI, impervious surface, and tree canopy cover. All variables were aggregated to their mean value within census block groups. Due to the likelihood of correlation across independent variables, single linear regressions were performed. Water and clouds were masked across all imagery prior to analysis. However, Landsat's accuracy in the recognition of all water pixels across imagery is less than 100% [92, 93]. To account for this and limit statistical analysis to land surfaces as best possible, census block groups with mean NDVI values of less than 0.1, a threshold most indicative of water-based pixels (e.g., clouds, shoreline or coastline) [94], were removed, leaving 1748 census block groups available for annual analysis (2013–2022). This process was repeated for seasonal analysis of NDVI.

To determine seasonal correlations with SAT (2015–2022), derived LST was compared to SAT observations in RStudio (Fig 3) [91]. On days where a Landsat image scene was captured, LST pixels were aggregated to their mean values within a 100-meter buffer around a weather station. Since Landsat imagery is captured at 11 AM ET/12 PM EST local time, LST was compared to 11 AM ET/12 PM EST SAT observations.

## 3. Results

### 3.1. LST climatology

Miami-Dade County's LST climatology reveals a unique annual pattern. During winter months (December to February), LST values are the lowest of the year on average (mean of Miami-Dade County's mean winter LST pixels = 18.51˚C) (Fig 6). Entering spring (March to May), mean LSTs increase as the northern hemisphere nears its June summer solstice (mean spring LST = 24.46˚C). Mean monthly LSTs peak in May before the peak in top of atmosphere solar insolation (June). This observed trend coincides with surface solar insolation (Fig 2B). April/May have the largest variability in monthly mean LST pixels across the county, as indicated by the box and whisker distributions in Fig 6 (difference between minimum and maximum mean monthly LST values). Summer (June to August) is characterized by a decrease in

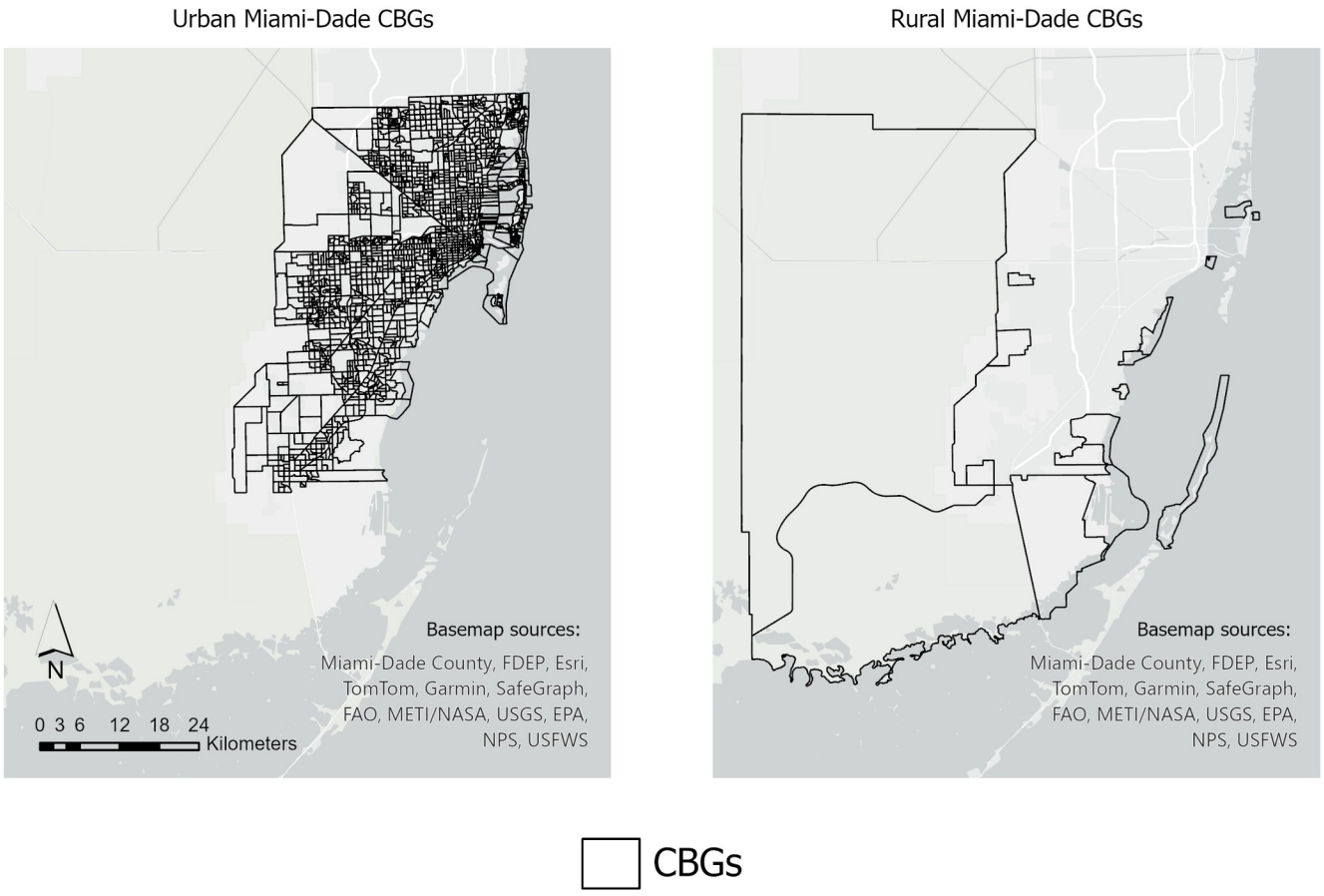


**Fig 5. Urban and rural Miami-Dade County census block groups (CBGs).** Urban CBGs (left) have greater than or equal to 5% mean imperviousness, while rural CBGs (right) have less than 5% mean imperviousness. Census block group shapefiles: U.S. Census Bureau [64]. Basemaps: ESRI [78, 79].

https://doi.org/10.1371/journal.pclm.0000278.g005

mean LST (mean summer LST = 24.20˚C). The fall months (September to November) depict a gradual decrease in average LSTs for the annual cycle as the year nears winter (mean LST = 21.94˚C). No significant trend exists in yearly mean LST over the study period. Yearly mean LST for Miami-Dade varies—2013 is the warmest year on average (23.69˚C), while 2021 is the coolest (20.76˚C).

A similar annual pattern is also present across mean census block group LST values in which utilized weather stations are located (Fig 7). Although there is variation across weather station mean LST values, mean LST peaks at each weather station in either April, May, or June, following the general mean Miami-Dade County LST trend (Fig 6). In addition, mean SAT values (at 11 AM ET/12 PM EST) at each weather station generally remain higher than mean LST values (at 11 AM ET/12 PM EST) annually, but the largest mean difference in the two measures of temperature exists during July, August, and September (summer and early fall) during the rainy season (Fig 2C).

## 3.2. Spatial analysis of LST

A prominent SUHI effect is visible within Miami-Dade County across the ten-year study period (Fig 8A). High levels of intraurban LST heterogeneity are visible throughout the

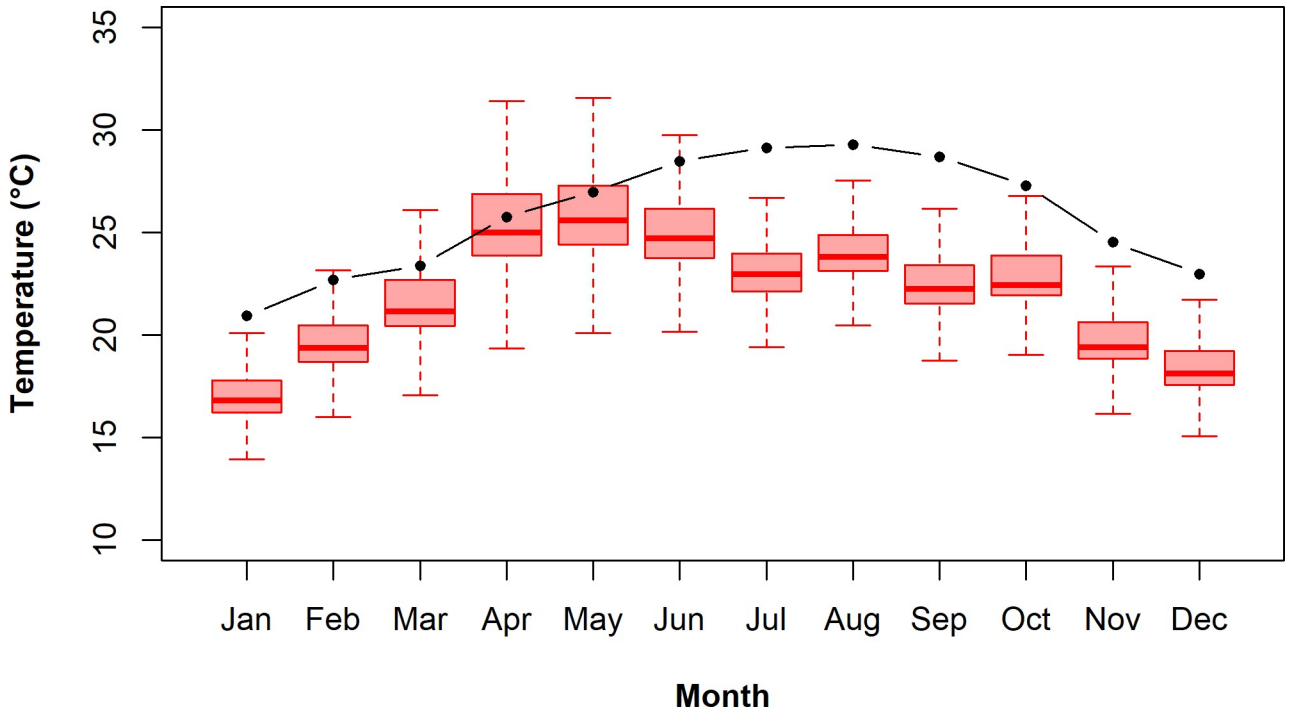


**Fig 6. Monthly LST (red) for Miami-Dade County and SAT (black) at KMIA.** For each monthly boxplot, LST pixels were averaged by month (2013–2022). Box and whiskers display the 1st, 25th, 75th, and 99th percentiles of monthly mean LST pixels, and the box line represents the median value. Each black dot represents monthly mean SAT at KMIA (2013–2022).

https://doi.org/10.1371/journal.pclm.0000278.g006

county's urban corridor, with areas of elevated LST that remain greater than 27˚C on average over 2013–2022. Such regions of elevated LST are over 2˚C warmer than the average urban LST and over 5˚C warmer than the entire county's average LST. These warm regions are most notably located along major roadways and other parts of the extensively developed landscape with low levels of greenness (Fig 8B). LSTs of 25˚C and higher, associated with extensive urban development, can be found as far south as 10–12 kilometers from the County's southern border, before transitioning into cooler LSTs as a result of wetlands and decreased urban surface.

The county's urban development boundary (Fig 1) to the west separates significantly warmer, urban development from the cooler, unchanged Everglades landscape (which accounts for most of the County's total land area at present). Urban Miami-Dade County exhibits an annual mean LST of 25.04˚C across the study period, considerably warmer than the rural region's annual mean LST (21.61˚C). This urban–rural difference in mean LSTs results in an annual mean SUHII of 3.43˚C across the study period. Mean SUHII varies expectedly with the seasons and is at its greatest during spring months (4.09˚C) when surface solar radiation is most intense (Fig 2B) and at its lowest during winter (2.95˚C) (Fig 9). Fall and summer mean SUHII remain near the average value, although fall's mean SUHII is greater than in the summer.

Biophysical drivers of spatial LST heterogeneity in Miami-Dade are shown in Fig 10. Results from regression analysis between LST and these variables are shown in Table 2. Mean NDVI values across the county are within ~0 to ~0.5 across the study period and have an inverse spatial relationship with LST values (Fig 8). As expected, annual mean NDVI per census block group across Miami-Dade has a negative relationship with annual mean LST per census block group (-8˚C per unit increase in NDVI, $p < 0.001$). The strength of this coefficient varies by season, at its strongest during spring (-10.5˚C per unit increase in NDVI,

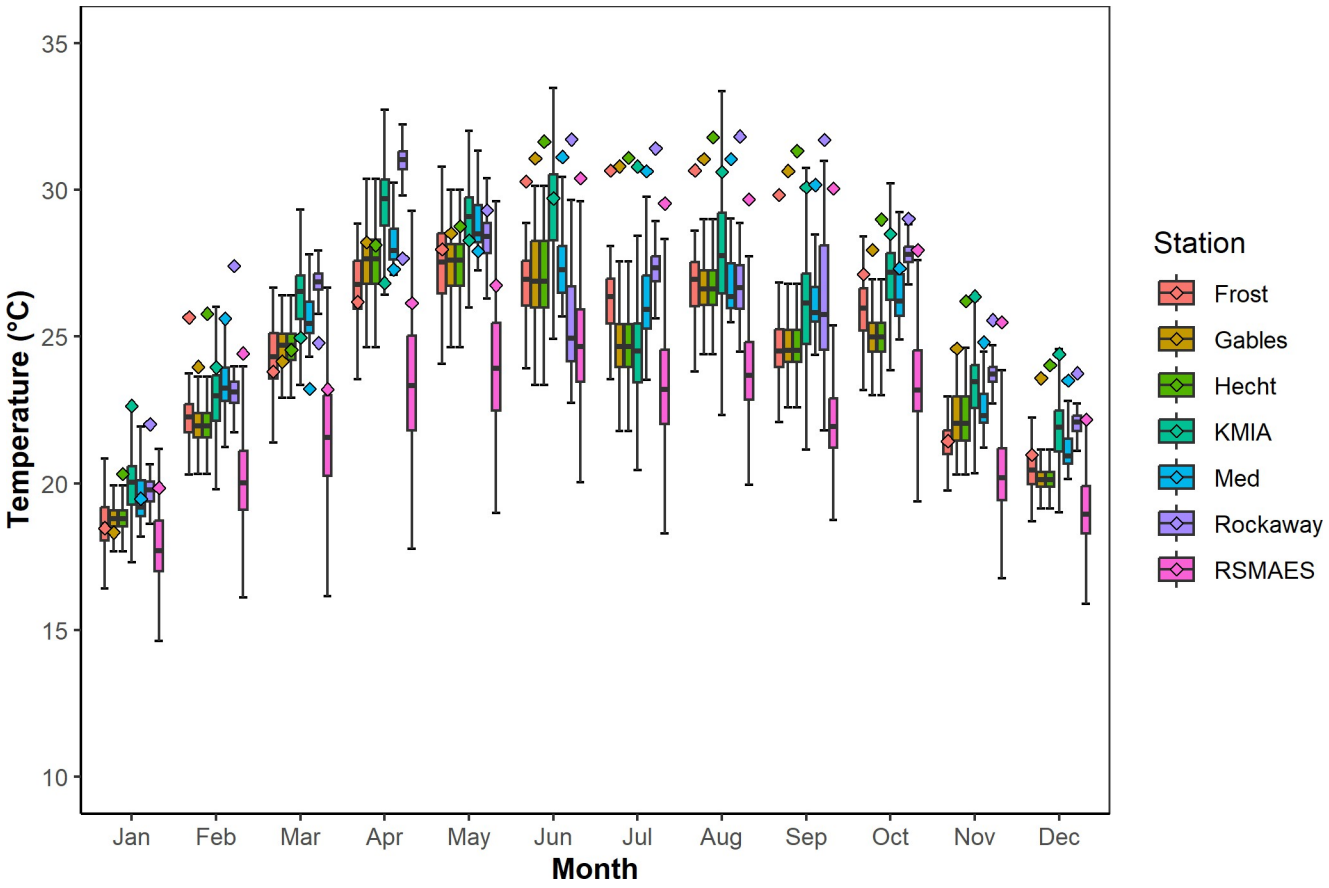


**Fig 7. Monthly LST for each weather station census block group (box plots) and SAT (diamonds) at weather stations (Fig 3).** For each monthly boxplot, LST pixels in each census block group in which there is a weather station were averaged across all monthly images (2013–2022). Box and whiskers display the 1st, 25th, 75th, and 99th percentiles of monthly mean LST pixels for each weather station census block group, and the box line represents the median value. Colored diamond shapes represent the average monthly SAT observed for the WeatherSTEM station within the respective census block group.

https://doi.org/10.1371/journal.pclm.0000278.g007

$p < 0.001$) and weakest during fall (-6.37˚C per unit increase in NDVI, $p < 0.001$) (Table 2). During April-June, when LST values are warmest, NDVI is also at peak values across the county. LSTs during these months in census block groups with the highest NDVI (upper decile) are upwards of 3˚C cooler than census block groups with the lowest NDVI (lower decile) (Fig 11). Similarly, percent tree canopy has a negative relationship with LST (-0.07˚C, $p < 0.001$). Tree canopy is also extremely heterogenous across the county. Across all county census block groups, percent tree canopy is on average 12.8%, with the majority of census block groups in Miami-Dade possessing 0–20%. Opposite of NDVI and tree canopy, mean impervious surface has a positive relationship with LST (0.05˚C per unit increase in impervious surface, $p < 0.001$), also seen in Fig 10. Miami-Dade County's urban corridor is characterized by extensive impervious surface: sprawling roadways, highways, and buildings (e.g., single-family residential, low to high rise, commercial, industrial) that are responsible for much of the elevated LSTs seen in Fig 8.

### 3.3. LST compared with SAT observations

Fig 12 shows the degree of agreement in LSTs and SATs across seasons by comparing mean census block group LST with available weather station SAT observations within that block

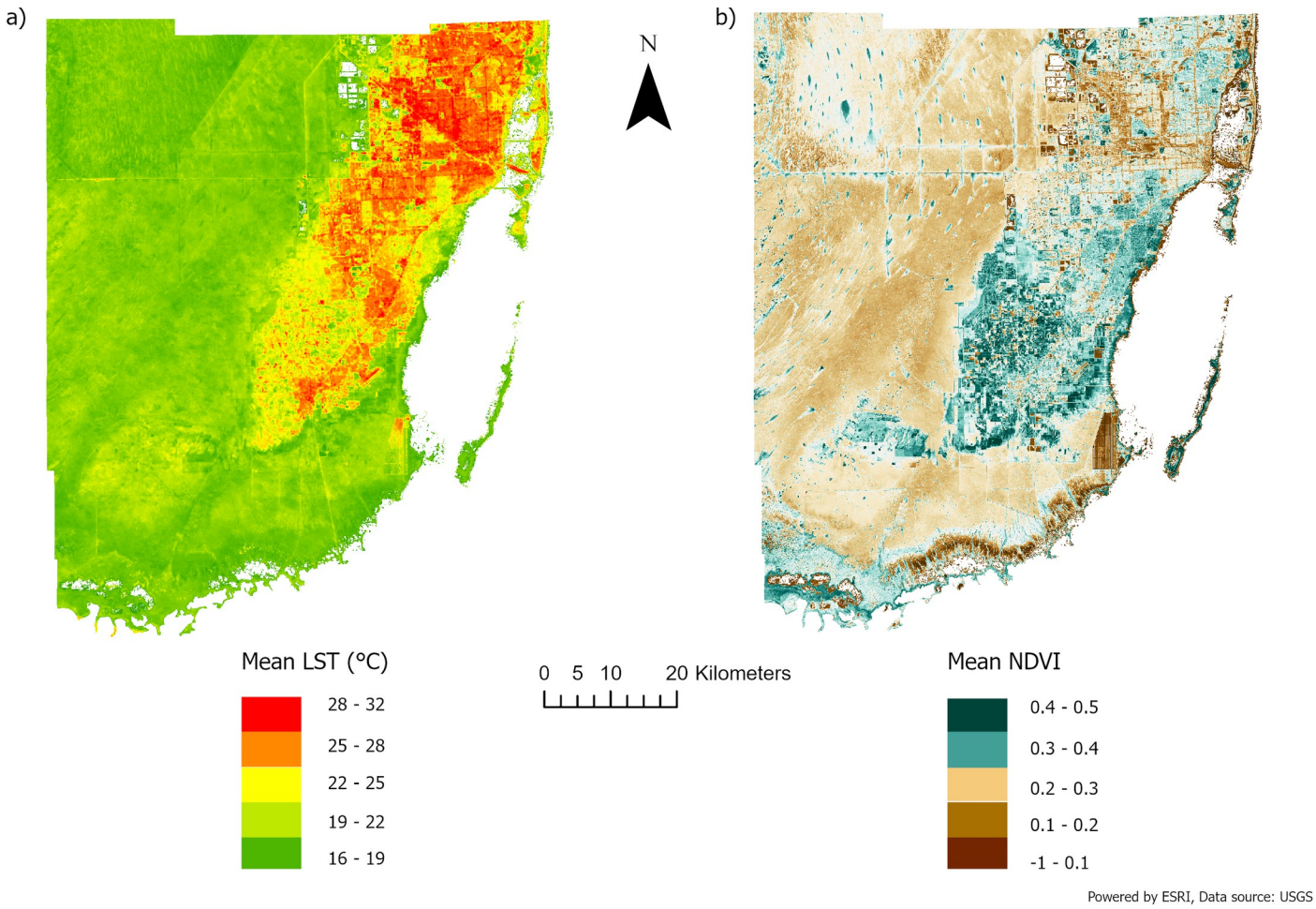


**Fig 8. Mean LST (˚C) and NDVI for Miami-Dade County (2013–2022).** (a) Each 30-by-30m pixel represents the mean LST value for all imagery (98 images) across the study period. The Miami-Dade SUHI is represented by yellow-to-red colors along the eastern portion of the county, as compared to more natural, preserved landscape where greener colors are observed. (b) Each 30-by-30m pixel represents the mean NDVI value for all imagery across the study period. Imagery data: USGS [75].

https://doi.org/10.1371/journal.pclm.0000278.g008

group (11 AM ET/12 PM EST, on the day of satellite image capture). During the winter months, LST and SAT exhibit a strong, positive correlation ($R = 0.91$, $p < 0.001$). In spring months there still exists a positive relationship, but a weaker, moderate correlation ($R = 0.59$, $p < 0.001$) as compared to winter. The relationship between LST and SAT during summer months is statistically insignificant ($p > 0.001$); however, subsequent fall months display a weaker relationship than both winter and spring ($R = 0.40$, $p < 0.001$). It is important to note, that unlike SAT in Fig 2A, mean monthly LSTs slightly decrease rather than increase in summer months July and August (Figs 6 and 7). The differences between daytime LST and SAT reach near 3˚C at their largest.

## 4. Discussion

LST plays a key role in lower atmosphere processes, including strongly influencing SAT, a key component of heat exposure [4, 5, 7, 26–34]. As such, LST's potential in serving as an accurate proxy for SAT can allow it to be a highly useful measure in identifying increased heat exposures across heterogenous urban regions [5, 6, 26, 36–44]. This accuracy, however, can depend

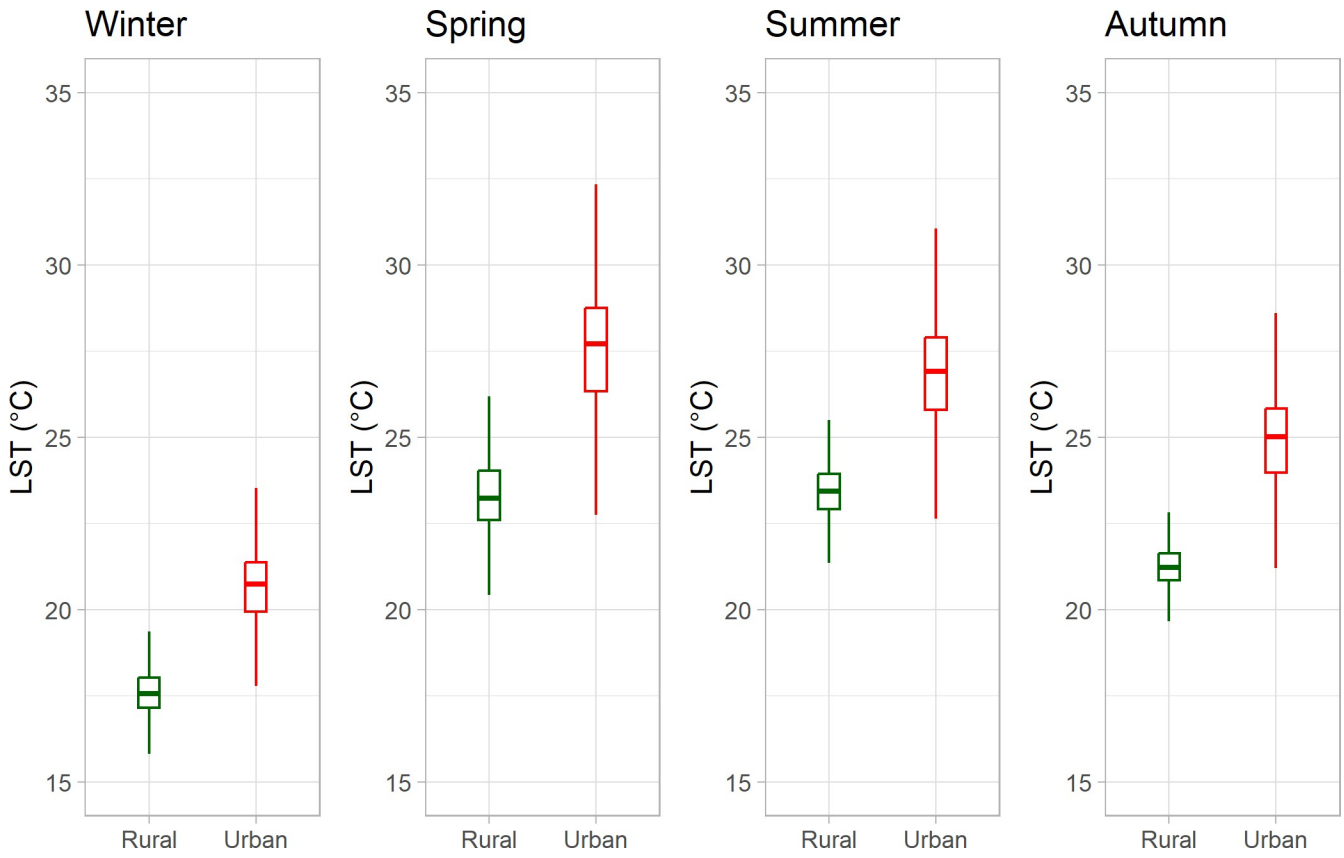


**Fig 9. Seasonal LST for the rural (green) and urban (red) region of Miami-Dade County (2013–2022).** For each boxplot, LST pixels were averaged by season within rural and urban regions of the county. Box and whiskers display the 1st, 25th, 75th, and 99th percentiles of seasonal rural and urban LST pixels. The box line represents the median.

https://doi.org/10.1371/journal.pclm.0000278.g009

on local mean climate. Here, we demonstrate this for a subtropical region that experiences a seasonally wet climate, using the case of Miami-Dade County, Florida. The results of this research show that, in this seasonally wet climate, daytime LST effectively characterizes spatial heterogeneity of the urban thermal landscape, including where heat exposures may be increased. Such intraurban heterogeneity is strongly linked to biophysical factors such as greenness and surface imperviousness. However, the strength of the relationship between daytime LST and SAT varies by season, indicating seasonal limitations in LST's use as a proxy for SAT and associated heat exposures. Although LST and SAT remain positively correlated annually, LST is limited in explaining SAT values during wet season months when SATs are highest, as it is not able to quantitatively capture SAT's magnitude.

The relationships found between LST and biophysical variables (NDVI, tree canopy, and impervious surface) in Miami-Dade County are consistent with the literature: we also find negative relationships with greenness and positive relationships with impervious surface [57, 95–98]. In this subtropical region with a seasonally wet climate, NDVI's negative relationship with LST changes by season and is most negative during spring (-10.5˚C per unit increase in NDVI, $p < 0.001$). Throughout spring months (March, April, May), NDVI values are at their highest alongside increased surface solar irradiance (Fig 2). This trend contrasts that of regions with arid climates, where the impact of minimal vegetation is frequently negligible or near zero [99]. In regions with more temperate climates, LST's relationship with NDVI fluctuates between positive in winter months and negative in summer months [100]. LST's relationship

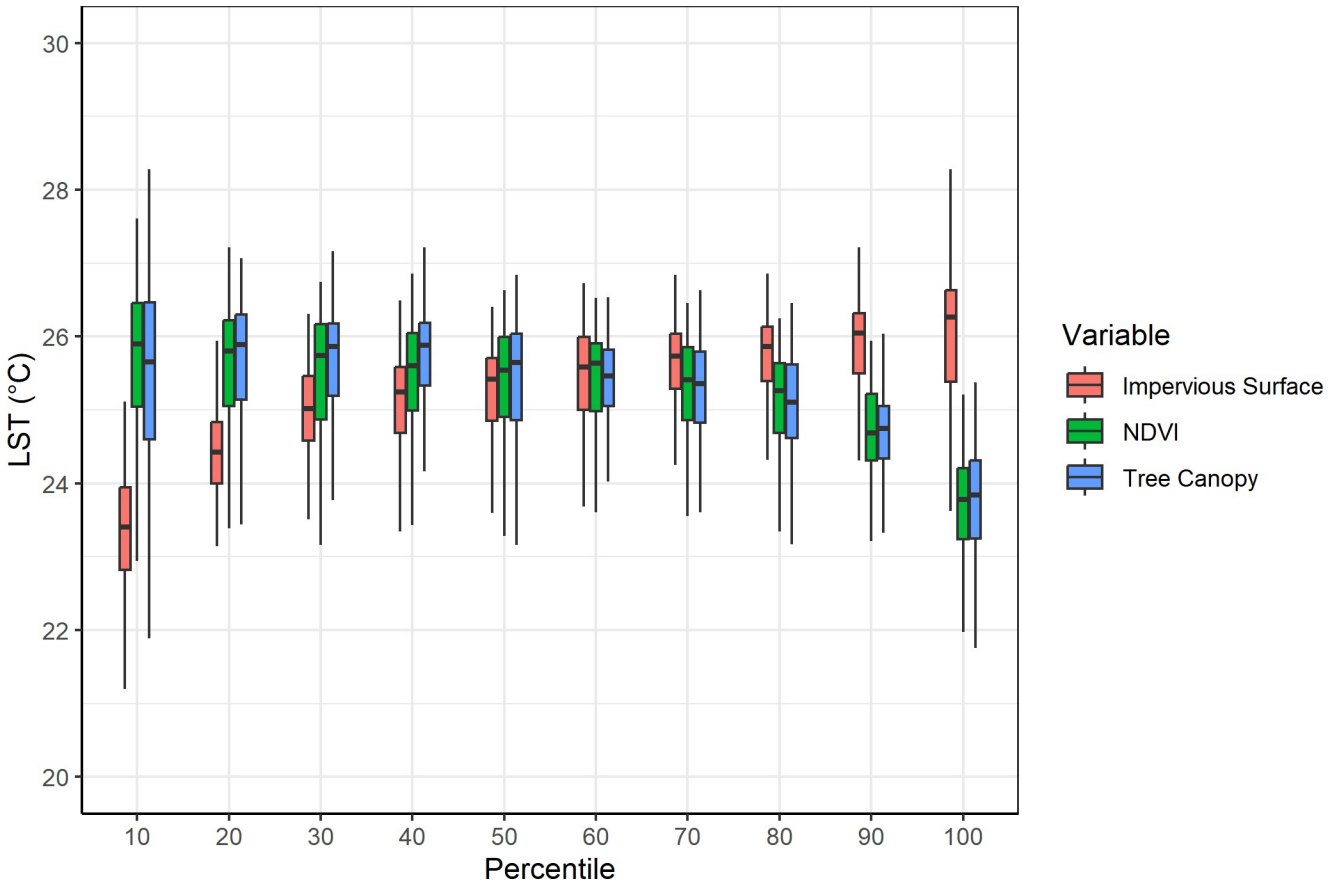


**Fig 10. Miami-Dade County mean LST per census block group ($n$ = 1748) by mean biophysical variable percentile.** For each box plot, annual mean LST pixels (2013–2022) were aggregated to the mean census block group value and binned (n ≈ 175 census block groups) by mean census block group percent impervious surface, NDVI, and percent tree canopy percentiles. Box and whiskers display the 1st, 25th, 75th, and 99th percentiles across annual mean census block group LST. The box line represents the median value.

https://doi.org/10.1371/journal.pclm.0000278.g010

with NDVI remains negative through all seasons in Miami-Dade County, highlighting the annual cooling impact of vegetation in a subtropical region that is warm year-round. Although negligible during certain seasons in temperate or arid climate types, such vegetation can be important in heat mitigation response in chronically warm subtropical-to-tropical regions, reducing the amount of radiation reaching the surface that can subsequently heat the lower atmosphere and increase local heat exposures [60, 61].

**Table 2. LST vs biophysical variables in Miami-Dade County.** The relationships between mean census block group (CBG) LST and mean CBG NDVI (including by season), mean CBG percent tree canopy, and mean CBG percent impervious surface are given for 1748 CBGs across the county. The coefficient can be interpreted as degree Celsius change per unit increase for a variable coefficient (e.g., a unit increase in mean impervious surface indicates a mean ~0.05 degree increase in LST).

| Variable (per CBG) | Coefficient (slope) | Std. Error | p-value (99% CI) | $R^2$ |
|---|---|---|---|---|
| Mean NDVI | -8.01 | 0.48 | $p < 0.001$ | ***0.14*** |
| Winter | -6.42 | 0.44 | $p < 0.001$ | 0.11 |
| Spring | -10.5 | 0.62 | $p < 0.001$ | 0.14 |
| Summer | -8.06 | 0.45 | $p < 0.001$ | 0.15 |
| Fall | -6.37 | 0.46 | $p < 0.001$ | 0.10 |
| Mean Percent Tree Canopy (%) | -0.07 | 0.003 | $p < 0.001$ | 0.19 |
| Mean Percent Impervious Surface (%) | 0.05 | 0.001 | $p < 0.001$ | 0.45 |

https://doi.org/10.1371/journal.pclm.0000278.t002

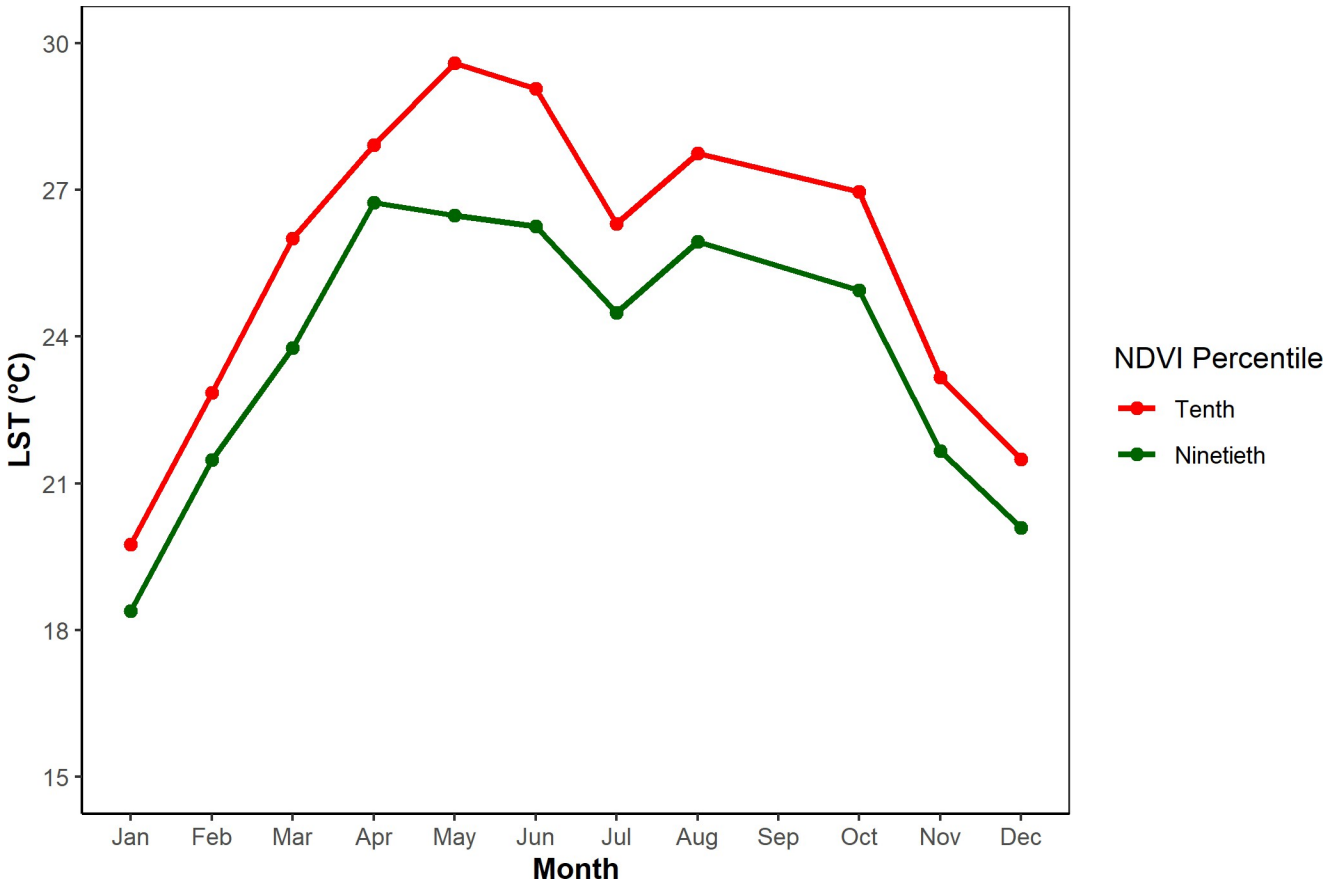


**Fig 11. Monthly mean LST by monthly tenth (red, low greenness) and monthly ninetieth (green, high greenness) NDVI percentiles.** LST and NDVI pixels were aggregated to their mean values within census block groups ($n$ = 1748) for each month (2013–2022). Data points represent the monthly mean LST values of Miami-Dade County census block groups at the monthly tenth NDVI percentile (red) and the monthly ninetieth NDVI percentile (green).

https://doi.org/10.1371/journal.pclm.0000278.g011

During winter, when monthly precipitation is at its minimum (Fig 2), LST and SAT exhibit a strong correlation with one another ($R$ = 0.91) (Fig 12), generally agreeing in magnitude. In contrast, during summer and fall months, the two measures exhibit a statistically insignificant relationship (summer, $p > 0.001$) and a weaker correlation (fall, $R$ = 0.40) respectively, as LST values were considerably lower than SAT values (up to 3˚C). Such a difference in LST and SAT, however, is smaller than that of a more temperate climate, in which the absolute difference in the two metrics during late morning was found to be upwards of 5˚C [101]. Time of day likely plays a role in LST being lower than SAT during summer months, as well as the magnitude of the LST/SAT difference, as the 11 AM ET/12 PM EST observations for LST do not capture surface heating near its peak [33, 49, 52]. Nonetheless, such a large disparity between LST and SAT during wet season months as compared to drier months at this time of day challenges the notion that the two heat metrics are spatiotemporally well correlated across all climate types [4, 5, 26–32]. This includes other subtropical regions with similar climates, in which strong correlations were found annually [58, 102, 103]. Although not comparing LST and SAT at the same time of day, other research has found similar fluctuations in the strength of the relationship between LST and SAT across seasons [48, 55]. Increased homogenization of surface conditions such as greenness during the winter (e.g., snow or ice in colder climates), likely shape LST's improved ability to capture SAT quantitatively outside of summer and fall months. In arid climates, such homogenous conditions (e.g., decreased greenness due to desert

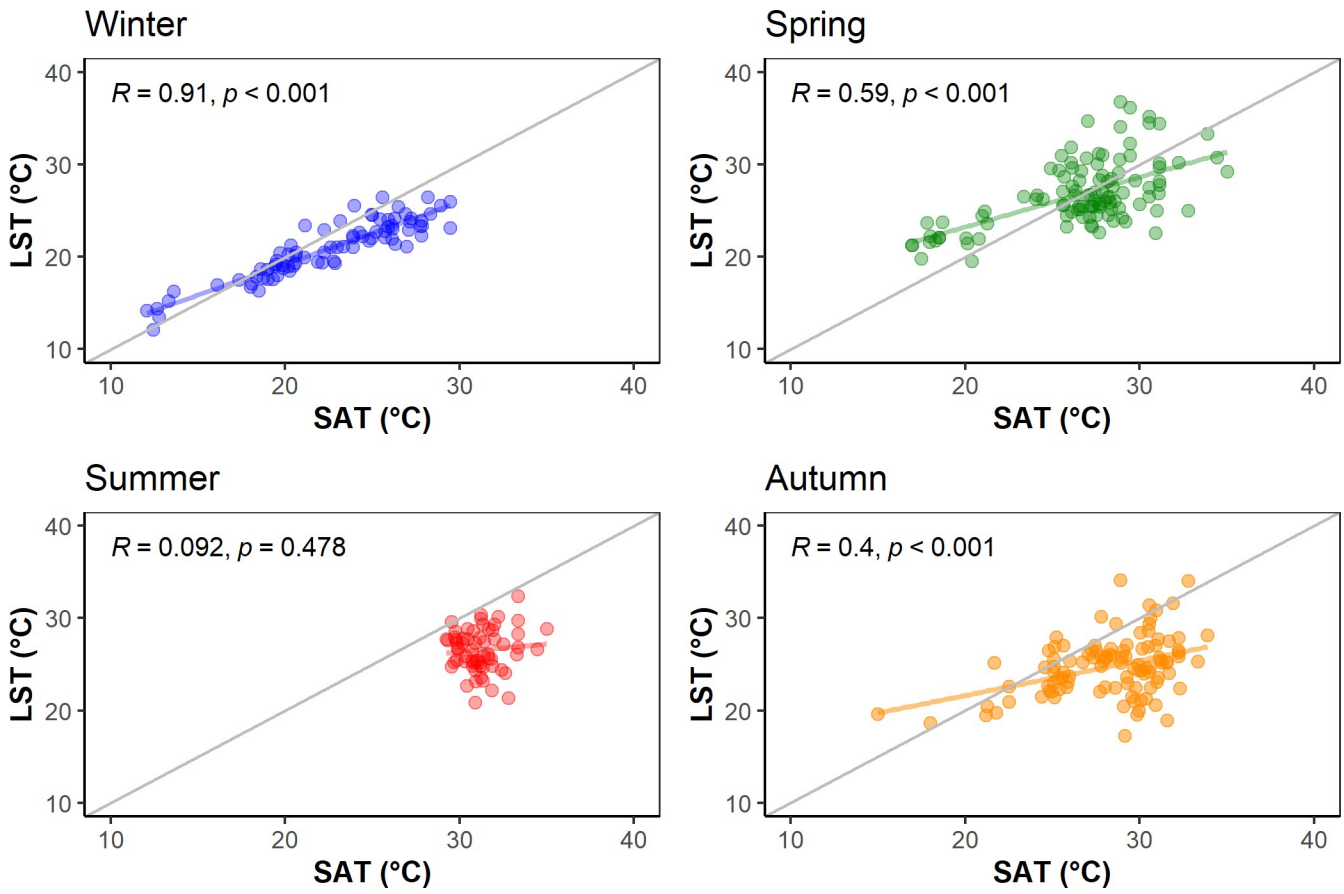


**Fig 12. Daily mean LST (within a 100-meter buffer) versus daily weather station SAT (˚C) (2013–2022).** LST imagery was captured at 11 AM ET/12 PM EST and was compared to 11 AM/12 PM EST SAT observations collected across seven weather stations (Fig 3) within Miami-Dade County [70, 77]. Each dot represents a single day and location.

https://doi.org/10.1371/journal.pclm.0000278.g012

biomes, etc.) persist for much of the year with minimal precipitation, allowing for a continuous, annual strong relationship between LST and SAT [104, 105]. Temperate and continental climate types at higher latitudes experience more moderate temperatures and considerably less solar radiation, allowing for smaller variation in LST and increased correlations with SAT [19, 33, 55, 56]. Thus, LST data can serve as a more accurate and effective, annual measure of heat exposures in these regions. However, in seasonally wet, tropical climates such as Miami-Dade's, where LST and SAT may not agree well across all seasons, LST cannot always serve as an accurate indicator of increased heat exposures. During summer and fall, if LST is used as a tool in decision-making around heat exposure, it must be recognized that the hazard could be significantly misrepresented. For example, as compared to winter months where LST can better capture SAT values, these findings suggest that LST may underestimate SAT by up to 3˚C during wet season months. During these times of year, additional data will be needed to fully understand the intensity of spatial heat risks to inform appropriate heat responses and adaptation strategies.

Miami-Dade's LST climatology reveals a unique annual pattern where on average, LST peaks in mid-to-late spring and early summer (April, May, June) (Fig 6). This early peak contrasts other urban regions across the northern hemisphere, where LST typically peaks in July/August alongside SAT [27, 36]. There are few comparable studies to understand whether this

pattern is characteristic of wet climates. In one example, Bechtel [36] noted a similar annual peak in Mexico City, where LST peaks in May prior to the onset of the wet season. However, unlike Miami-Dade, SAT in Mexico City annually peaks concurrent with local mean LST. This suggests that the later SAT peak in Miami-Dade County (as compared to LST) may be a feature that is unique locally, implying the existence of factors other than atmospheric conditions controlling the seasonality of the two heat metrics (e.g., geography, elevation, latitude, proximity to coastlines) [32, 34, 48, 106]. In addition, the intensity of the SUHI phenomenon in Miami-Dade County follows the trend of annual LST. SUHII is greatest in spring months, rather than summer months, also contrasting SUHIIs of most urban regions across the northern hemisphere [16, 17, 25, 107].

Geography also appears to play a key role in SUHII, which was of smaller magnitude in Miami-Dade County as compared to other urban regions globally, including subtropical and tropical urban regions. Urban Miami-Dade exhibited a mean SUHII of 3.43˚C warmer than rural Miami-Dade across the study period. Miami-Dade's rural areas are composed of mostly water and small vegetation (e.g., grasses, mangroves, shrubs) in wetlands or marshes of the Everglades. Such an urban–rural geography reduces SUHII, as compared to other wet, urban regions including Medellín, Colombia, and São Paulo, Brazil, that are surrounded more dense vegetation or forest and exhibit mean annual daytime SUHIIs above 5˚C [17, 88]. All types of rural areas with increased greenness (as compared to urban areas) evaporatively cool faster and more effectively than adjacent urban surfaces. However, forests and dense canopied regions are more capable of converting incoming solar radiation to latent heat through transpiration, resulting in a more prominent SUHI phenomenon [47, 58, 59, 108]. Miami-Dade's limited canopy in rural areas results in a smaller difference between urban and rural LSTs, compared to other urban-rural regions of the subtropics and tropics (e.g., Medellín, Colombia; São Paulo, Brazil; etc.), as well as more continental and temperate regions with extensive forest biomes [47, 54, 88]. Because rural areas with less canopy cover (such as Miami-Dade's Everglades) exhibit higher LSTs, these rural areas provide less heat relief from urban LSTs. For regions across the subtropics and tropics with consistent heat hazards and minimal rural tree canopy, urban tree canopy remains an important consideration for heat mitigation, as rural areas may not provide significant heat relief.

Several limitations exist for this study. First, cloud cover significantly limited the number of scenes captured by satellite imagery. The average number of pixels across Miami-Dade monthly average LST imagery was 5,704,452—while the average number of pixels across summer months that were most likely to be affected by increased cloud cover was 5,453,231. Analyzed LST imagery also does not account for cloud shadows that cast over regions and potentially decrease observed LST values [109]. Although improving, the Landsat QA_PIXEL band, utilized for the recognition of clouds and land cover types, remains limited its accuracy in identifying pixels associated with certain land cover types (e.g., water, clouds, mixed land/water such as shorelines) [92, 93]. Thus, the masking of all water and cloud pixels for analysis is not fully accurate. Second, impervious surface and tree canopy are static observations that were captured at a specific time during the study period. Thus, impervious surface and tree canopy from 2013 and 2014, respectively, may not accurately represent LST values from different times throughout the study period, as land use and land cover have changed over time. To account for this as best as possible, impervious surface and tree canopy data were averaged across available datasets (impervious surface, 2013–2021; tree canopy, 2013–2021). Third, weather stations that collect unofficial SAT observations are not registered with the National Weather Service (apart from KMIA) and lack official quality control. The quantity of stations across Miami-Dade County with regular surface observations is also limited. Because SAT is greatly influenced by hyperlocal conditions, additional weather stations and improved station

networks with more recorded observations can help to increase accuracy in the assessment of LST and SAT relationships [110]. Lastly, for the purposes of this study, to access more abundant imagery and maintain higher resolution LST data, images from 11 AM ET/12 PM EST were used. Thus, LST values are not indicative of the daily maximum, as daytime surface heating from solar radiation is not yet at its peak. Additional LST imagery captured over time, and at different times of day, will also aid in analyzing the relationship between LST and SAT throughout the course of the day, as well as the continued assessment of the Miami-Dade County SUHI phenomenon.

## 5. Conclusions

Using the case of Miami-Dade County, Florida, this study evaluated the accuracy of LST as a proxy for SAT in a subtropical urban region with a seasonally wet, tropical climate. Importantly, we find that LST has a different temporal relationship with SAT as compared to better studied temperate regions. These results raise important considerations for urban heat adaptation and planning: in subtropical-to-tropical regions with seasonally wet climates, LST remains a proxy for the spatial patterns of SAT, however, its accuracy in capturing the magnitude of SAT is limited annually. LST may mispresent the heat exposures people experience across the urban region during the wet season, as in this case study, LST underestimated SAT during wet season months at this time of observation (11 AM ET/12 PM EST). Heat exposure within chronically hot humid climates is an increasing public health emergency, both within the study area and across subtropical-to-tropical regions of the globe. Urban adaptation planning to date has largely drawn upon LST to inform heat responses across neighborhoods, but use of LST alone may mischaracterize the most acute heat exposures, underestimating their magnitudes both across neighborhoods and during the peak of the heat season, especially in climates with tropical characteristics. Our results therefore have immediate relevance to ongoing heat-adaptation decision-making. They simultaneously establish key areas that are important for future research inquiries, including understanding the role of localized processes that may affect surface energy balances and resulting LST values.

## Supporting information

**S1 Table. List of collected LST imagery dates and breakdown of LST scenes by month and year (2013–2022).**
(XLSX)

## Acknowledgments

Maps and figures throughout this article (Figs 1, 3–5 and 8) were created using ArcGIS® software by Esri. ArcGIS® and ArcMap™ are the intellectual property of Esri and are used herein under license. Copyright © Esri. All rights reserved. For more information about Esri® software, please visit www.esri.com.

Figs 2, 6, 7 and 9–12 were created using the ggplot2 package (https://ggplot2.tidyverse.org) in RStudio software.

## Author Contributions

**Conceptualization:** Nkosi Muse, Amy Clement, Katharine J. Mach.

**Data curation:** Nkosi Muse.

**Formal analysis:** Nkosi Muse.

**Investigation:** Nkosi Muse.

**Methodology:** Nkosi Muse, Amy Clement, Katharine J. Mach.

**Software:** Nkosi Muse.

**Supervision:** Katharine J. Mach.

**Validation:** Nkosi Muse.

**Visualization:** Nkosi Muse.

**Writing – original draft:** Nkosi Muse.

**Writing – review & editing:** Amy Clement, Katharine J. Mach.

## References

1. Kim J-P, Guldmann J-M. Land-use planning and the urban heat island. Environ Plan B Plan Des. 2014; 41: 1077–1099. https://doi.org/10.1068/b130091p
2. Wu H, Ye L-P, Shi W-Z, Clarke KC. Assessing the effects of land use spatial structure on urban heat islands using HJ-1B remote sensing imagery in Wuhan, China. Int J Appl Earth Obs Geoinformation. 2014; 32: 67–78. https://doi.org/10.1016/j.jag.2014.03.019
3. Tadros W, Naguib Wellenstein S, Das A, B Palmarini M, D'Aoust N, Severine Singh O, et al. Demographic trends and urbanization. The World Bank; 2021 Apr. Report No.: 158009. Available: https://documents1.worldbank.org/curated/en/260581617988607640/pdf/Demographic-Trends-and-Urbanization.pdf
4. Terjung WH, Louie SS-F. Solar radiation and urban heat islands. Ann Assoc Am Geogr. 1973; 63: 181–207. https://doi.org/10.1111/j.1467-8306.1973.tb00918.x
5. Asaeda T, Ca VT, Wake A. Heat storage of pavement and its effect on the lower atmosphere. Atmos Environ. 1996; 30: 413–427. https://doi.org/10.1016/1352-2310(94)00140-5
6. Oke TR. The energetic basis of the urban heat island. Q J R Meteorol Soc. 1982; 108: 1–24. https://doi.org/10.1002/qj.49710845502
7. Sekertekin A, Zadbagher E. Simulation of future land surface temperature distribution and evaluating surface urban heat island based on impervious surface area. Ecol Indic. 2021; 122: 107230. https://doi.org/10.1016/j.ecolind.2020.107230
8. Buyantuyev A, Wu J. Urban heat islands and landscape heterogeneity: linking spatiotemporal variations in surface temperatures to land-cover and socioeconomic patterns. Landsc Ecol. 2010; 25: 17–33. https://doi.org/10.1007/s10980-009-9402-4
9. Wilson B. Urban heat management and the legacy of redlining. J Am Plann Assoc. 2020; 86: 443–457. https://doi.org/10.1080/01944363.2020.1759127
10. Li Z-L, Tang B-H, Wu H, Ren H, Yan G, Wan Z, et al. Satellite-derived land surface temperature: Current status and perspectives. Remote Sens Environ. 2013; 131: 14–37. https://doi.org/10.1016/j.rse.2012.12.008
11. Zhou D, Xiao J, Bonafoni S, Berger C, Deilami K, Zhou Y, et al. Satellite remote sensing of surface urban heat islands: progress, challenges, and perspectives. Remote Sens. 2019; 11: 48. https://doi.org/10.3390/rs11010048
12. Huang G, Zhou W, Cadenasso ML. Is everyone hot in the city? Spatial pattern of land surface temperatures, land cover and neighborhood socioeconomic characteristics in Baltimore, MD. J Environ Manage. 2011; 92: 1753–1759. https://doi.org/10.1016/j.jenvman.2011.02.006 PMID: 21371807
13. Méndez-Lázaro P, Muller-Karger FE, Otis D, McCarthy MJ, Rodríguez E. A heat vulnerability index to improve urban public health management in San Juan, Puerto Rico. Int J Biometeorol. 2017; 1–14. https://doi.org/10.1007/s00484-017-1319-z PMID: 28210860
14. Gu Y, Li D. A modeling study of the sensitivity of urban heat islands to precipitation at climate scales. Urban Clim. 2018; 24: 982–993. https://doi.org/10.1016/j.uclim.2017.12.001
15. Ojeh VN, Balogun AA, Okhimamhe AA. Urban-rural temperature differences in Lagos. Climate. 2016; 4: 29. https://doi.org/10.3390/cli4020029
16. Manoli G, Fatichi S, Bou-Zeid E, Katul GG. Seasonal hysteresis of surface urban heat islands. Proc Natl Acad Sci. 2020; 117: 7082–7089. https://doi.org/10.1073/pnas.1917554117 PMID: 32184330

17. Peng S, Piao S, Ciais P, Friedlingstein P, Ottle C, Bréon F-M, et al. Surface urban heat island across 419 global big cities. Environ Sci Technol. 2012; 46: 696–703. https://doi.org/10.1021/es2030438 PMID: 22142232

18. Haashemi S, Weng Q, Darvishi A, Alavipanah SK. Seasonal variations of the surface urban heat island in a semi-arid city. Remote Sens. 2016; 8: 352. https://doi.org/10.3390/rs8040352

19. Wu X, Wang G, Yao R, Wang L, Yu D, Gui X. Investigating surface urban heat islands in South America based on MODIS data from 2003–2016. Remote Sens. 2019; 11: 1212. https://doi.org/10.3390/rs11101212

20. Lemoine-Rodríguez R, Inostroza L, Zepp H. Intraurban heterogeneity of space-time land surface temperature trends in six climate-diverse cities. Sci Total Environ. 2022; 804: 150037. https://doi.org/10.1016/j.scitotenv.2021.150037 PMID: 34509842

21. Ogunjobi KO, Adamu Y, Akinsanola AA, Orimoloye IR. Spatio-temporal analysis of land use dynamics and its potential indications on land surface temperature in Sokoto Metropolis, Nigeria. R Soc Open Sci. 2018;5. https://doi.org/10.1098/rsos.180661 PMID: 30662716

22. Doll D, Ching JKS, Kaneshiro J. Parameterization of subsurface heating for soil and concrete using net radiation data. Bound-Layer Meteorol. 1985; 32: 351–372. https://doi.org/10.1007/BF00122000

23. Yuvaraj D P G, Jayachandran K, Al-Quraishi A. Color slices analysis of land use changes due to urbanization in a city environment of Miami Area, South Florida, USA. Model Earth Syst Environ. 2021;7. https://doi.org/10.1007/s40808-020-00883-x

24. Athukorala D, Murayama Y. Spatial variation of land use/cover composition and impact on surface urban heat Island in a tropical sub-saharan city of Accra, Ghana. Sustainability. 2020; 12: 7953. https://doi.org/10.3390/su12197953

25. Zhou D, Zhao S, Liu S, Zhang L, Zhu C. Surface urban heat island in China's 32 major cities: spatial patterns and drivers. Remote Sens Environ. 2014; 152: 51–61. https://doi.org/10.1016/j.rse.2014.05.017

26. Hulley GC, Ghent D, Göttsche FM, Guillevic PC, Mildrexler DJ, Coll C. 3—Land surface temperature. In: Hulley GC, Ghent D, editors. Taking the Temperature of the Earth. Elsevier; 2019. pp. 57–127. https://doi.org/10.1016/B978-0-12-814458-9.00003–4

27. Jin M, Dickinson RE. Land surface skin temperature climatology: benefitting from the strengths of satellite observations. Environ Res Lett. 2010; 5: 044004. https://doi.org/10.1088/1748-9326/5/4/044004

28. Yao R, Luo Q, Li B. A simplified mathematical model for urban microclimate simulation. Build Environ. 2011; 46: 253–265. https://doi.org/10.1016/j.buildenv.2010.07.019

29. Yao R, Wang L, Huang X, Zhang W, Li J, Niu Z. Interannual variations in surface urban heat island intensity and associated drivers in China. J Environ Manage. 2018; 222: 86–94. https://doi.org/10.1016/j.jenvman.2018.05.024 PMID: 29804036

30. Stone B, Frumkin H, Hess JJ. Urban form and extreme heat events: are sprawling cities more vulnerable to climate change Than compact cities? Environ Health Perspect. 2010; 118: 1425–1428. https://doi.org/10.1289/ehp.0901879 PMID: 21114000

31. Sánchez JM, Coll C, Niclòs R. Remote sensing monitoring of land surface temperature (LST). MDPI, Basel; 2021. https://doi.org/10.3390/books978-3-0365-1427-7

32. Chakraborty TC, Newman AJ, Qian Y, Hsu A, Sheriff G. Residential segregation and outdoor urban moist heat stress disparities in the United States. One Earth. 2023; 6: 738–750. https://doi.org/10.1016/j.oneear.2023.05.016

33. Zeng L, Wardlow B, Tadesse T, Shan J, Hayes M, Li D, et al. Estimation of daily air temperature based on MODIS land surface temperature products over the Corn Belt in the US. Remote Sens. 2015; 7: 951–970. https://doi.org/10.3390/rs70100951

34. Chung J, Lee Y-G, Jang W, Lee S, Kim S. Correlation analysis between air temperature and MODIS land surface temperature and prediction of air temperature using TensorFlow long short-term memory for the period of occurrence of cold and heat waves. Remote Sens. 2020; 12: 3231. https://doi.org/10.3390/rs12193231

35. Shandas V, Voelkel J, Williams J, Hoffman J. Integrating Satellite and Ground Measurements for Predicting Locations of Extreme Urban Heat. Climate. 2019; 7: 5. https://doi.org/10.3390/cli7010005

36. Bechtel B. A new global climatology of annual land surface temperature. Remote Sens. 2015; 7: 2850–2870. https://doi.org/10.3390/rs70302850

37. Tomlinson CJ, Chapman L, Thornes JE, Baker C. Remote sensing land surface temperature for meteorology and climatology: a review. Meteorol Appl. 2011; 18: 296–306. https://doi.org/10.1002/met.287

38. Licker R, Dahl K, Abatzoglou JT. Quantifying the impact of future extreme heat on the outdoor work sector in the United States. Elem Sci Anthr. 2022; 10: 00048. https://doi.org/10.1525/elementa.2021.00048

39. Rogers CDW, Ting M, Li C, Kornhuber K, Coffel ED, Horton RM, et al. Recent increases in exposure to extreme humid-heat events disproportionately affect populated regions. Geophys Res Lett. 2021; 48: e2021GL094183. https://doi.org/10.1029/2021GL094183

40. Hoehne CG, Hondula DM, Chester MV, Eisenman DP, Middel A, Fraser AM, et al. Heat exposure during outdoor activities in the US varies significantly by city, demography, and activity. Health Place. 2018; 54: 1–10. https://doi.org/10.1016/j.healthplace.2018.08.014 PMID: 30199773

41. Weber S, Sadoff N, Zell E, de Sherbinin A. Policy-relevant indicators for mapping the vulnerability of urban populations to extreme heat events: A case study of Philadelphia. Appl Geogr. 2015; 63: 231–243. https://doi.org/10.1016/j.apgeog.2015.07.006

42. Muse N, Iwaniec DM, Wyczalkowski C, Mach KJ. Heat exposure and resilience planning in Atlanta, Georgia. Environ Res Clim. 2022; 1: 015004. https://doi.org/10.1088/2752-5295/ac78f9

43. Tuholske C, Caylor K, Funk C, Verdin A, Sweeney S, Grace K, et al. Global urban population exposure to extreme heat. Proc Natl Acad Sci. 2021;118. https://doi.org/10.1073/pnas.2024792118 PMID: 34607944

44. Chakraborty T, Hsu A, Manya D, Sheriff G. Disproportionately higher exposure to urban heat in lower-income neighborhoods: a multi-city perspective. Environ Res Lett. 2019; 14: 105003. https://doi.org/10.1088/1748-9326/ab3b99

45. Liu X, Zhou Y, Yue W, Li X, Liu Y, Lu D. Spatiotemporal patterns of summer urban heat island in Beijing, China using an improved land surface temperature. J Clean Prod. 2020; 257: 120529. https://doi.org/10.1016/j.jclepro.2020.120529

46. Jin M, Dickinson RE, Vogelmann AM. A Comparison of CCM2–BATS Skin Temperature and Surface-Air Temperature with Satellite and Surface Observations. J Clim. 1997; 10: 1505–1524. https://doi.org/10.1175/1520-0442(1997)010<1505:ACOCBS>2.0.CO;2

47. Imhoff ML, Zhang P, Wolfe RE, Bounoua L. Remote sensing of the urban heat island effect across biomes in the continental USA. Remote Sens Environ. 2010; 114: 504–513. https://doi.org/10.1016/j.rse.2009.10.008

48. Zhang P, Bounoua L, Imhoff ML, Wolfe RE, Thome K. Comparison of MODIS land surface temperature and air temperature over the continental USA meteorological stations. Can J Remote Sens. 2014; 40: 110–122. https://doi.org/10.1080/07038992.2014.935934

49. Pepin NC, Maeda EE, Williams R. Use of remotely sensed land surface temperature as a proxy for air temperatures at high elevations: Findings from a 5000 m elevational transect across Kilimanjaro. J Geophys Res Atmospheres. 2016; 121: 9998. https://doi.org/10.1002/2016JD025497

50. Kakoniti A, Georgiou G, Marakkos K, Kumar P, Neophytou MK -a. The role of materials selection in the urban heat island effect in dry mid-latitude climates. Environ Fluid Mech. 2016; 16: 347–371. https://doi.org/10.1007/s10652-015-9426-z

51. Song J, Wang Z-H, Myint SW, Wang C. The hysteresis effect on surface-air temperature relationship and its implications to urban planning: An examination in Phoenix, Arizona, USA. Landsc Urban Plan. 2017; 167: 198–211. https://doi.org/10.1016/j.landurbplan.2017.06.024

52. Goldblatt R, Addas A, Crull D, Maghrabi A, Levin GG, Rubinyi S. Remotely Sensed Derived Land Surface Temperature (LST) as a Proxy for Air Temperature and Thermal Comfort at a Small Geographical Scale. Land. 2021; 10: 410. https://doi.org/10.3390/land10040410

53. Mutiibwa D, Strachan S, Albright T. Land Surface Temperature and Surface Air Temperature in Complex Terrain. IEEE J Sel Top Appl Earth Obs Remote Sens. 2015; 8: 4762–4774. https://doi.org/10.1109/JSTARS.2015.2468594

54. Wu X, Zhang L, Zang S. Examining seasonal effect of urban heat island in a coastal city. PLoS ONE. 2019; 14: e0217850. https://doi.org/10.1371/journal.pone.0217850 PMID: 31199819

55. Burnett M, Chen D. The Impact of Seasonality and Land Cover on the Consistency of Relationship between Air Temperature and LST Derived from Landsat 7 and MODIS at a Local Scale: A Case Study in Southern Ontario. Land. 2021; 10: 672. https://doi.org/10.3390/land10070672

56. Shandas V, Makido Y, Upraity A. Evaluating Differences between Ground-Based and Satellite-Derived Measurements of Urban Heat: The Role of Land Cover Classes in Portland, Oregon and Washington, D.C. Land. 2023. https://doi.org/10.3390/land12030562

57. Sheng L, Tang X, You H, Gu Q, Hu H. Comparison of the urban heat island intensity quantified by using air temperature and Landsat land surface temperature in Hangzhou, China. Ecol Indic. 2017; 72: 738–746. https://doi.org/10.1016/j.ecolind.2016.09.009

58. Chakraborty T, Sarangi C, Tripathi SN. Understanding diurnality and inter-seasonality of a sub-tropical urban heat island. Bound-Layer Meteorol. 2017; 163: 287–309. https://doi.org/10.1007/s10546-016-0223-0

59. Zhao L, Lee X, Smith RB, Oleson K. Strong contributions of local background climate to urban heat islands. Nature. 2014; 511: 216–219. https://doi.org/10.1038/nature13462 PMID: 25008529

60. Zhang K, Cao C, Chu H, Zhao L, Zhao J, Lee X. Increased heat risk in wet climate induced by urban humid heat. Nature. 2023; 1–5. https://doi.org/10.1038/s41586-023-05911-1 PMID: 37100919

61. Raymond C, Matthews T, Horton RM, Fischer EM, Fueglistaler S, Ivanovich C, et al. On the Controlling Factors for Globally Extreme Humid Heat. Geophys Res Lett. 2021; 48: e2021GL096082. https://doi.org/10.1029/2021GL096082

62. US Census Bureau. QuickFacts: Miami-Dade County, Florida. In: United States Census Bureau [Internet]. [cited 16 Jan 2023]. Available: https://www.census.gov/quickfacts/fact/table/miamidadecountyflorida/POP060210

63. Beck HE, McVicar TR, Vergopolan N, Berg A, Lutsko NJ, Dufour A, et al. High-resolution (1 km) Köppen-Geiger maps for 1901–2099 based on constrained CMIP6 projections. Sci Data. 2023; 10: 724. https://doi.org/10.1038/s41597-023-02549-6 PMID: 37872197

64. US Census Bureau. TIGER/Line Shapefiles. In: United States Census Bureau [Internet]. [cited 30 Nov 2023]. Available: https://www.census.gov/geographies/mapping-files/2020/geo/tiger-line-file.html

65. County Miami-Dade. Data, Maps, and Apps. In: Open Data Hub [Internet]. [cited 20 May 2024]. Available: https://gis-mdc.opendata.arcgis.com/

66. GloH2O. Köppen-Geiger Global 1-km climate classification maps. 2 Mar 2021 [cited 21 Jun 2024]. Available: https://www.gloh2o.org/koppen/

67. Florida Climate Center. Miami Weather Planner. In: Florida State University Florida Climate Center [Internet]. 2023 [cited 6 Apr 2022]. Available: https://climatecenter.fsu.edu/products-services/data/weather-planner/miami

68. National Oceanic and Atmospheric Administration. U.S. Climate Normals. In: National Centers for Environmental Information (NCEI) [Internet]. 2023 [cited 6 Apr 2023]. Available: https://www.ncei.noaa.gov/products/land-based-station/us-climate-normals

69. Winsberg MD. Climate of Florida. In: Florida Climate Center [Internet]. 2011. Available: https://climatecenter.fsu.edu/images/fcc/climateofflorida.pdf

70. WeatherSTEM. WeatherSTEM Portal for Miami Dade County, Florida. In: Miami-Dade WeatherSTEM [Internet]. 2023 [cited 15 May 2023]. Available: https://miamidade.weatherstem.com/

71. PRISM Climate Group. Time Series Values for Individual Locations. In: Northwest Alliance for Computational Science and Engineering [Internet]. 2023 [cited 1 May 2018]. Available: http://www.prism.oregonstate.edu/explorer/

72. Daly C, Halbleib M, Smith JI, Gibson WP, Doggett MK, Taylor GH, et al. Physiographically sensitive mapping of climatological temperature and precipitation across the conterminous United States. Int J Climatol. 2008; 28: 2031–2064. https://doi.org/10.1002/joc.1688

73. Sánchez-Aparicio M, Andrés-Anaya P, Del Pozo S, Lagüela S. Retrieving land surface temperature from satellite Imagery with a novel combined strategy. Remote Sens. 2020; 12: 277. https://doi.org/10.3390/rs12020277

74. USGS. USGS EROS Archive—Landsat Archives—Landsat 8 OLI (Operational Land Imager) and TIRS (Thermal Infrared Sensor) Level-1 Data Products. In: Earth Resources Observation and Science (EROS) Center [Internet]. Oct 2019. Available: https://www.usgs.gov/centers/eros/science/usgs-eros-archive-landsat-archives-landsat-8-oli-operational-land-imager-and?qt-science_center_objects=0#qt-science_center_objects

75. USGS. EarthExplorer. In: United States Geological Survey [Internet]. 2023 [cited 20 Oct 2019]. Available: https://earthexplorer.usgs.gov/

76. National Aeronautics and Space Administration. The Worldwide Reference System. In: Landsat Science [Internet]. 30 Nov 2021 [cited 22 Mar 2024]. Available: https://landsat.gsfc.nasa.gov/about/the-worldwide-reference-system/

77. Iowa State University. Iowa State University Iowa Environmental Mesonet. In: ASOS-AWOS-METAR Data Download [Internet]. 2023 [cited 14 Dec 2023]. Available: https://mesonet.agron.iastate.edu/request/download.phtml?network=FL_ASOS

78. ESRI. World Basemap v2 "Light Grey Base." Available: https://cdn.arcgis.com/sharing/rest/content/items/291da5eab3a0412593b66d384379f89f/resources/styles/root.json

79. ESRI. Terms of use for static maps. In: ArcGIS Online [Internet]. [cited 12 Jul 2024]. Available: https://doc.arcgis.com/en/arcgis-online/reference/static-maps.htm

80. National Land Cover Database. Data. In: Multi-Resolution Land Characteristics Consortium [Internet]. 2023 [cited 23 Jun 2023]. Available: https://www.mrlc.gov/data

81. Muse NM. Ten-year land surface temperature (LST) climatology of Miami-Dade County Florida (2013–2022)—University of Miami. 2024. https://doi.org/10.17604/9bef-2d86

82. Avdan U, Jovanovska G. Algorithm for automated mapping of land surface temperature using Landsat 8 satellite data. J Sens. 2016; 2016: 1–8. https://doi.org/10.1155/2016/1480307

83. Environmental Systems Research Institute (Esri). ArcGIS Pro. Redlands, CA; 2021.

84. Jiang F. Evaluation of stray light correction for the thermal infrared sensor (TIRS) from Landsat 8. Rochester Institute of Technology. 2017. Available: https://scholarworks.rit.edu/theses/9606/

85. Weier J, Herring D. Measuring Vegetation (NDVI & EVI). In: NASA Earth Observatory [Internet]. NASA Earth Observatory; 30 Aug 2000 [cited 1 Jul 2022]. Available: https://earthobservatory.nasa.gov/features/MeasuringVegetation

86. Missions Landsat. Landsat Collection 2 Quality Assessment Bands. In: USGS [Internet]. [cited 6 Jun 2024]. Available: https://www.usgs.gov/landsat-missions/landsat-collection-2-quality-assessment-bands

87. Yang J, Zhan Y, Xiao X, Xia JC, Sun W, Li X. Investigating the diversity of land surface temperature characteristics in different scale cities based on local climate zones. Urban Clim. 2020; 34: 100700. https://doi.org/10.1016/j.uclim.2020.100700

88. Yao R, Wang L, Huang X, Gong W, Xia X. Greening in rural areas increases the surface urban heat island Intensity. Geophys Res Lett. 2019; 46: 2204–2212. https://doi.org/10.1029/2018GL081816

89. US Census Bureau. Urban and Rural. In: United States Census Bureau [Internet]. [cited 10 May 2024]. Available: https://www.census.gov/programs-surveys/geography/guidance/geo-areas/urban-rural.html

90. Florida Audubon. Urban Development Boundary Expansion Halted–For Now–In Miami-Dade County. In: Everglades [Internet]. 30 May 2023 [cited 10 May 2024]. Available: https://fl.audubon.org/news/urban-development-boundary-expansion-halted-%E2%80%93-now-%E2%80%93-miami-dade-county

91. Posit team. RStudio: Integrated Development for R. Boston, MA: PBC; 2024. Available: http://www.posit.co/

92. Frantz D. FORCE—Landsat + Sentinel-2 Analysis Ready Data and Beyond. Remote Sens. 2019; 11: 1124. https://doi.org/10.3390/rs11091124

93. Qiu S, Lin Y, Shang R, Zhang J, Ma L, Zhu Z. Making Landsat Time Series Consistent: Evaluating and Improving Landsat Analysis Ready Data. Remote Sens. 2019; 11: 51. https://doi.org/10.3390/rs11010051

94. Hashim H, Abd Latif Z, Adnan NA. URBAN VEGETATION CLASSIFICATION WITH NDVI THRESHOLD VALUE METHOD WITH VERY HIGH RESOLUTION (VHR) PLEIADES IMAGERY. Int Arch Photogramm Remote Sens Spat Inf Sci. 2019;XLII–4/W16: 237–240. https://doi.org/10.5194/isprs-archives-XLII-4-W16-237-2019

95. Yue W, Xu J, Tan W, Xu L. The relationship between land surface temperature and NDVI with remote sensing: application to Shanghai Landsat 7 ETM+ data. Int J Remote Sens. 2007; 28: 3205–3226. https://doi.org/10.1080/01431160500306906

96. Khan Z, Javed A. Correlation between land surface temperature (LST) and normalized difference vegetation index (NDVI) in Wardha Valley Coalfield, Maharashtra, Central India. Nova Geod. 2022; 2: 53–53. https://doi.org/10.55779/ng2353

97. Guha S, Govil H. Land surface temperature and normalized difference vegetation index relationship: a seasonal study on a tropical city. SN Appl Sci. 2020; 2: 1661. https://doi.org/10.1007/s42452-020-03458-8

98. Yuan F, Bauer ME. Comparison of impervious surface area and normalized difference vegetation index as indicators of surface urban heat island effects in Landsat imagery. Remote Sens Environ. 2007; 106: 375–386. https://doi.org/10.1016/j.rse.2006.09.003

99. Julien Y, Sobrino J, Mattar C, Ruescas A, Jimenez J-C, Sòria Barres G, et al. Temporal analysis of NDVI and LST parameters to detect changes in the Iberian land cover between 1981 and 2001. Int J Remote Sens. 2011; 32: 2057–2068.

100. Sun D, Kafatos M. Note on the NDVI-LST relationship and the use of temperature-related drought indices over North America. Geophys Res Lett. 2007;34. https://doi.org/10.1029/2007GL031485

101. Berg E, Kucharik C. The Dynamic Relationship between Air and Land Surface Temperature within the Madison, Wisconsin Urban Heat Island. Remote Sens. 2021; 14: 165. https://doi.org/10.3390/rs14010165

102. do Nascimento ACL, Galvani E, Gobo JPA, Wollmann CA. Comparison between air temperature and land surface temperature for the city of São Paulo, Brazil. Atmosphere. 2022; 13: 491. https://doi.org/10.3390/atmos13030491

**103.** Gusso A, Fontana DC, Gonçalves GA. Mapeamento da temperatura da superfície terrestre com uso do sensor AVHRR/NOAA. Pesqui Agropecuária Bras. 2007; 42: 231–237. https://doi.org/10.1590/S0100-204X2007000200012

**104.** Cohen J, Screen JA, Furtado JC, Barlow M, Whittleston D, Coumou D, et al. Recent Arctic amplification and extreme mid-latitude weather. Nat Geosci. 2014; 7: 627–637. https://doi.org/10.1038/ngeo2234

**105.** Coumou D, Di Capua G, Vavrus S, Wang L, Wang S. The influence of Arctic amplification on mid-latitude summer circulation. Nat Commun. 2018; 9: 2959. https://doi.org/10.1038/s41467-018-05256-8 PMID: 30127423

**106.** Azevedo JA, Chapman L, Muller CL. Quantifying the daytime and night-time urban heat island in Birmingham, UK: a comparison of satellite derived land surface temperature and high resolution air temperature observations. Remote Sens. 2016; 8: 153. https://doi.org/10.3390/rs8020153

**107.** Dian C, Pongrácz R, Dezső Z, Bartholy J. Annual and monthly analysis of surface urban heat island intensity with respect to the local climate zones in Budapest. Urban Clim. 2020; 31: 100573. https://doi.org/10.1016/j.uclim.2019.100573

**108.** Mildrexler DJ, Zhao M, Running SW. A global comparison between station air temperatures and MODIS land surface temperatures reveals the cooling role of forests. J Geophys Res Biogeosciences. 2011;116. https://doi.org/10.1029/2010JG001486

**109.** Wang T, Shi J, Ma Y, Husi L, Comyn-Platt E, Ji D, et al. Recovering land surface temperature under cloudy skies considering the solar-cloud-satellite geometry: application to MODIS and Landsat-8 data. J Geophys Res Atmospheres. 2019; 124: 3401–3416. https://doi.org/10.1029/2018JD028976

**110.** Clement A, Troxler T, Keefe O, Arcodia M, Cruz M, Hernandez A, et al. Hyperlocal observations reveal persistent extreme urban heat in southeast Florida. J Appl Meteorol Climatol. 2023;1. https://doi.org/10.1175/JAMC-D-22-0165.1